Geostatistical analysis of soil gas data in a high seismic intermontane basin: Fucino Plain, central Italy

G. Ciotoli,[1] S. Lombardi,[1] and A. Annunziatellis[1]

Received 13 September 2005; revised 22 September 2006; accepted 27 October 2006; published 10 May 2007.

[1] Numerous soil gas measurements of four gaseous species with very different geochemical behaviors were performed in the Fucino Basin, an area characterized by known and inferred structural discontinuities. A comprehensive statistical and geostatistical treatment of these data followed in order to provide insight into the spatial influence of tectonic discontinuities and geology on deep-seated gas migration toward the surface. The results yielded anomalies with different features, reflecting the different gas-bearing properties of the eastern seismogenic faults related to the 1915 earthquake (M_b = 7.0) and the hidden structural features occurring in the western side of the plain. In particular, this approach demonstrates that soil gas concentration (i.e., Rn and CO_2) can identify the simpler normal faults of the eastern sector of the plain. In contrast, the more pervasive fracturing and faulting, as well as the occurrence of coarser deposits, on the western side of the area, make the location of faults less clear. The results show that gases migrate preferentially through zones of brittle deformation by advective processes, as suggested by the relatively high rate of migration needed to obtain anomalies of short-lived ^{222}Rn in the soil pores. Furthermore, a geostatistical study of soil gas data was conducted to quantify the spatial domain of correlation and the gas-bearing properties of faults on the basis of shallow soil gas distribution (i.e., anisotropic behavior). The results provide a clear correlation between the shape and orientation of the anomalies and the different geometry of the faults recognized in the plain.

Citation: Ciotoli, G., S. Lombardi, and A. Annunziatellis (2007), Geostatistical analysis of soil gas data in a high seismic intermontane basin: Fucino Plain, central Italy, *J. Geophys. Res.*, *112*, B05407, doi:10.1029/2005JB004044.

1. Introduction

[2] Distinguishing an ‘‘active fault’’ from one which is ‘‘inactive’’ is one of the most important problems of neotectonics because of the seismic hazard commonly associated with fault activity. Although the term active fault is in current use, no definition is universally accepted, because the adopted criteria are based on the tectonic setting and style of seismicity of an area, and on the specific target of study (e.g., seismic zonation for an urban settlement). In general, scientists define as active those faults showing (1) evidence of historical and/or instrumental seismic activity and/or (2) stratigraphic/morphologic displacements within a time period which can span from the Holocene (10,000 years) to the entire Quaternary period [*Slemmons and McKinney*, 1977; *Vittori et al.*, 1991].

[3] *Azzaro et al.* [1998] argue that the concept of fault activity appears too generic when dealing with hazard evaluation, and that a more useful term is fault capability as applied to a subset of active faults with evidence of surface slip and therefore those which are potentially most harmful [*Slemmons and McKinney*, 1977].

[1]Dipartimento di Scienze della Terra, Università di Roma ‘‘La Sapienza,’’ Rome, Italy.

0148-0227/07/2005JB004044$09.00

[4] Not all capable faults are directly evident on surface (especially where the sedimentation rates on the fault trace is higher than the slip rate) and thus geophysical and geochemical methods are necessary for their detection. Moreover, it is important to remember that fault slip behavior is often complicated by the mixture of two end-member styles: stick slip (coseismic fast slip) and stable sliding (continuous slow creep), which can occur in different sections of the same fault or alternating in time. While the first tends to rejuvenate and keep the fracture network open near the fault, the second allows for crystallization and hence fault self-sealing.

[5] Recent advances in the study of fluid geochemistry (i.e., soil gas surveys) related to structural geology have shown the potential of this method for studying both fault activity and seismic hazard [*Lombardi et al.*, 1999; *Ciotoli et al.*, 1999, 1998]. The importance of fluid geochemistry is rooted in the fact that the Earth is an open system and that fluid-releasing crustal phenomena are a major means for the exchange of matter and energy at different depths. As such, fluid-releasing channels like active faults and fractures are actually a ‘‘window’’ on subterranean physical and chemical variations, as well as seismotectonic processes.

[6] In terms of seismicity, degassing has been shown to occur mainly by advection in fractured areas and/or free gas phase release from mineral springs due to the pressure drop

which occurs during ascent of the fluid toward surface [*Toutain and Baubron*, 1999]. In particular, moderate to large earthquakes cause pore pressure changes along fracture and fault surfaces, resulting in sharp variations in the movement and concentration of some gaseous species due to the evolution of the local stress regime, particularly evident when the seismic event is approaching (i.e., dilatancy and related phenomena: for a detailed review, see *Sibson* [1990], *Zhang and Sanderson* [1996], and *Hickman et al.* [1995]).

[7] On the basis of these variations, a geochemically active fault zone has been defined as a wide belt characterized by high geochemical contrast (either in space or time) with respect to the surrounding geochemical "background" [*Ciotoli et al.*, 2005, 1998; *King et al.*, 1996; *Zhang and Sanderson*, 1996; *Zhiguan*, 1991; *Sugisaki*, 1983]. In this sense an active fault zone (defined in a strictly tectonic sense by paleoseismology and/or neotectonics), may or may not correspond to a geochemically active fault zone.

[8] It has been shown that the permeability of the fault gouge and highly fractured zones generate complex geochemical patterns in the soil air [*Ciotoli et al.*, 2005, 1998; *King et al.*, 1996; *Zhang and Sanderson*, 1996; *Zhiguan*, 1991; *Sugisaki*, 1983]. Generally, all types of faults should be considered as anomalous for fluxes and concentrations of all types of gases [*Klusman*, 1993]. This characteristic has been used to highlight active faults by using radon emanation from soil, but also using CO_2, He and H_2 distribution in the shallow environment.

[9] Field data have shown the usefulness of the soil gas method for detecting crustal discontinuities even when faults are buried or cut noncohesive clastic rocks, which makes surface recognition difficult using traditional field methods [*Ciotoli et al.*, 1998; *Lombardi et al.*, 1996; *Duddridge et al.*, 1991; *Durrance and Gregory*, 1988]. These characteristics, the rapidity and the low cost of the soil gas survey, make this method a powerful tool for geological investigation which can significantly contribute to seismic hazard assessment and to seismic forecasting when continuous monitoring is performed [*Klusman*, 1993; *Reimer*, 1990; *King et al.*, 1996; *Sugisaki*, 1983].

[10] Soil gas distribution is also affected by surface features such as pedological, biogenic, and meteorological factors; however, these are expected to have a subordinate effect on gas leakage from deep faults. To best understand the system as a whole, however, it is necessary to study the association of various gases, to collect a large number of samples during periods of stable meteorological and soil moisture conditions (e.g., during the dry season), and to statistically treat the data using appropriate methods. In this study we analyzed radiogenic trace gases (He and Rn) and "diagenetic" gases (CO_2 and CH_4) which act as carriers for the trace gases in an effort to understand what information soil gas geochemistry can give regarding the location, activity, and tectonic style of faults.

[11] The Fucino basin (central Italy) was chosen as a test site because it displays a network of surface and shallow active faults within the valley floor that were partially reactivated during the 1915 Avezzano earthquake (Ms = 7.0) [*Oddone*, 1915].

[12] In detail, the primary goals of this study are (1) to test the sensitivity of the soil gas method for locating fault or fracture systems masked by plastic, unconsolidated lithologies (e.g., lacustrine clays); (2) to investigate the gas-bearing properties (i.e., gas associations and their spatial correlation) of visible and/or hidden faults (recognized by geophysical surveys); (3) to apply geostatistical methods in order to study the influence of the spatial domain of these faults on the gas distribution (i.e., anomaly shape, extent and trend); and (4) to evaluate the link between the sampling density (regional and detailed) and the spatial distribution of soil gas anomalies.

2. Geostatistics

[13] Geostatistics offers a group of methods to quantitatively describe the spatial continuity that is an essential feature of many natural phenomena [*Ciotoli and Finoia*, 2005; *Houlding*, 2000; *Goovaerts*, 1997; *Deutsch and Journel*, 1997; *Krajevskj and Gibbs*, 1996; *Pannatier*, 1996; *Isaaks and Mohan Srivastava*, 1989; *Journel*, 1987]. For the application of this methodology two assumptions are required: (1) spatial stationarity, which assumes that the studied variables remain constant across the investigated area; and (2) ergodicity, which assumes that the spatial statistics measured across the investigated area are unbiased estimates of the studied variables [*Matheron*, 1971].

[14] In geostatistics, modeling of spatial data is accomplished through the calculation of the experimental variogram, showing the increase in variability between sample locations as distance between the samples increases [*Tobler*, 1970]. The variogram describes the spatial relationship between the sample values as a function that relates the variance (γ) to the distance of sample separations, usually called lag (h). The variogram equation is given as

$$\gamma(h) = \frac{1}{2n}\sum_{x=1}^{n}[Z(x) - Z(x+h)]^2 \quad (1)$$

where $\gamma(h)$ is the semivariance, $Z(x)$ and $Z(x + h)$ are the observation values of the studied variable measured at point x and at a point separated by h, respectively, and n is the numbers of sample pairs.

[15] Two-dimensional variograms (i.e., the variogram surface) are usually displayed as contour lines and can be useful for revealing anisotropy in the data. The anisotropy of the variogram surface reveals a covariance structure (values tend to be more similar in one or more preferred directions than in others) that is usually related to the orientation of natural phenomena acting in the studied area.

[16] The experimental variogram is commonly fitted by using a mathematical equation whose main parameters (i.e., sill, range, and nugget) are used to calculate values at unsampled locations via interpolation. In the field of Earth sciences kriging is one of the most commonly used estimation technique that uses variogram model parameters [*Stein*, 1999; *Krige*, 1966].

[17] Kriging is a linear interpolation technique that uses randomly distributed measured data, x_i, to predict (interpolate/extrapolate) values at any unsampled location within the area of interest. This prediction makes use of the spatial dependencies of the measured values. This technique is

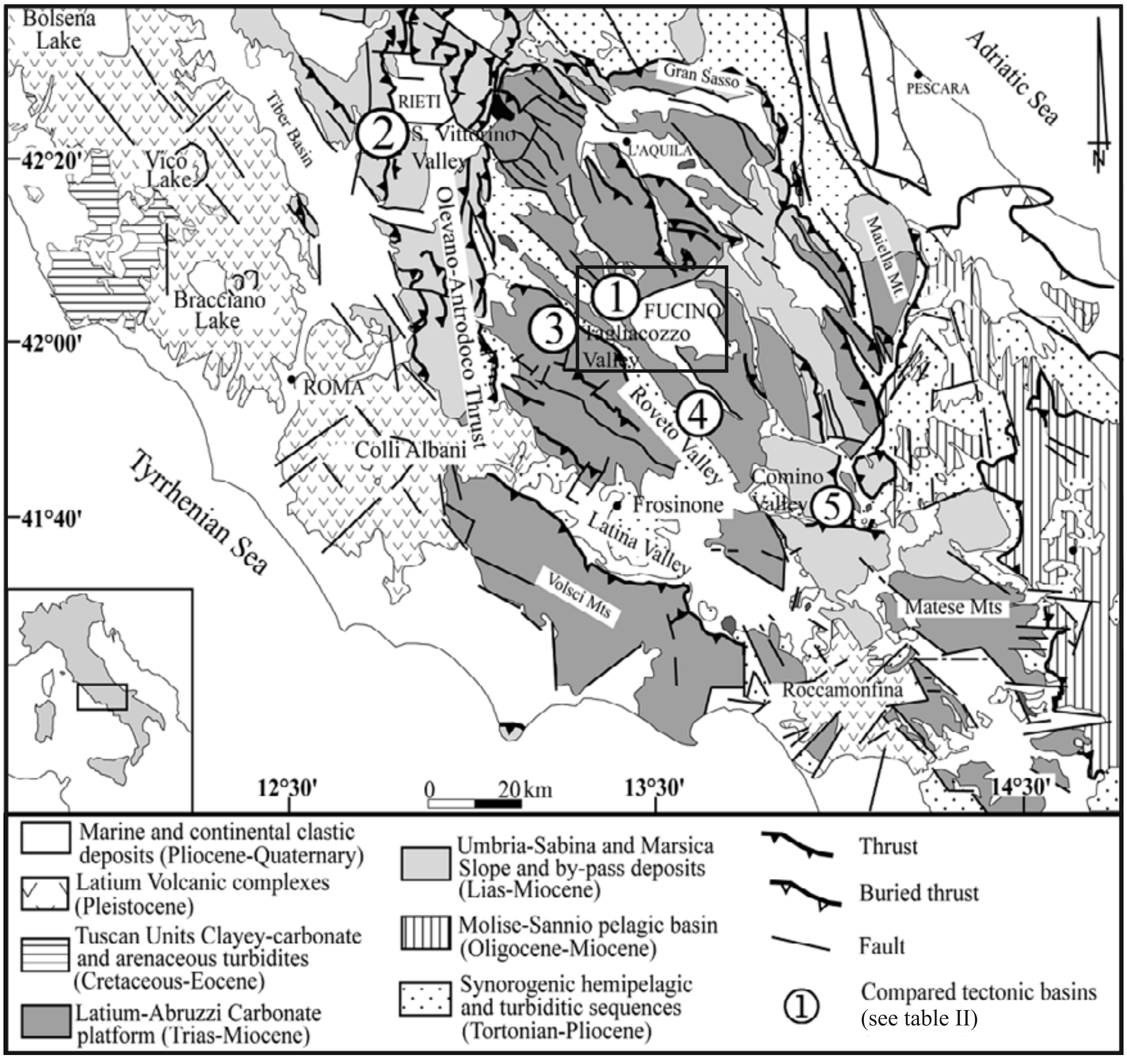

Figure 1. Generalized geologic and structural map of the central Apennines [*Cavinato and De Celles*, 1999]. Numbers indicate radon data from other investigated intermontane basins compared in the Table 1.

often associated with the acronym BLUE for best linear unbiased estimator of the unknown parameters being studied; "linear" because its estimates are weight-linear combinations of the available data, "unbiased" since it tries to have the mean residual or error equal to 0, and "best" because it aims at minimizing the variance of the errors [see *Goovaerts*, 1997; *Krajevskj and Gibbs*, 1996; *Isaaks and Mohan Srivastava*, 1989; *Journel*, 1987; *Matheron*, 1971; *Krige*, 1966].

[18] In this work geostatistical analysis was performed to investigate the presence of phenomena acting along specific directions (e.g., fault-related anisotropy effect). The geostatistical approach consisted of the following tasks: (1) construction of experimental directional variograms to investigate the spatial dependency of gas concentrations (i.e., calculate the main variogram parameters: nugget, range, and sill); (2) determination of directional differences (anisotropy) which are important for defining the anisotropy parameters for the kriging estimation (i.e., directions and ratio between the major and minor anisotropy ellipse axes); and (3) estimation of the spatial distribution of the studied variables using variogram model parameters in the kriging algorithm to construct contour maps.

3. Geological and Structural Setting

[19] The Fucino basin is a rombhoidal intermontane tectonic depression located in the middle of Apennine mountains (central Italy) (Figure 1), a Cenozoic thrust and fold belt which is has been undergoing uplift and extension since the late Pliocene [*Cavinato et al.*, 2002; *Cavinato and De Celles*, 1999; *Galadini and Galli*, 1999; *Galadini et al.*, 1997; *Blumetti et al.*, 1993, 1988; *Mostardini and Merlini*, 1988; *Bally et al.*, 1986]. During the Quaternary the basin has been generally deprived of a natural outlet and has hosted a wide lake (artificially drained in the second half of 19th century [*Giraudi*, 1989]), thus collecting a thick sequence of Pleistocene and Holocene silty lacustrine deposits interbedded with coarse alluvial fan deposits at its borders. The long-lasting activity of the normal faults bordering the basin [*Cavinato et al.*, 2002; *Galadini et al.*, 1997; *Michetti et al.*, 1996] is testified by the terraced

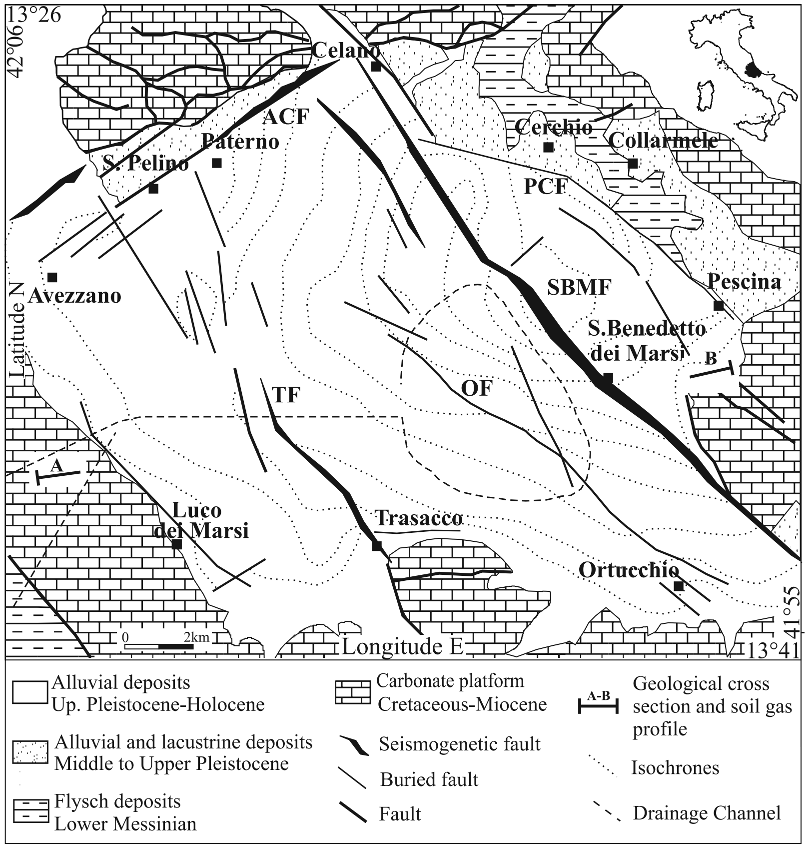

Figure 2. Detailed geological map of the Fucino basin. The map shows the main buried and/or visible faults in the plain, the trace of the geological and soil gas profile cross section (A-B), as well as the isochron contour map (interval 100 ms) of the alluvial and lacustrine deposits that represents the isopach map of the sedimentary cover [*Cavinato et al.*, 2002; *Ciotoli et al.*, 1998].

middle-upper Pleistocene alluvial fan and fluvial-lacustrine deposits hanging for hundreds of meters above the present valley floor in the north and northeastern borders of the basin, the thickness and geometry of the buried sediments, and the high and rectilinear mountain fronts [*Bosi et al.*, 1995; *Giraudi*, 1989].These faults are part of a fault and seismicity belt extending along the mountain chain from the northern Apennines to Calabria, with major earthquakes having magnitudes >6.5 [*Vittori*, 1994].

[20] The main faults (Figure 2) recognized in the Fucino basin are (1) the Tre Monti (TMF) and Avezzano-Celano (ACF-inferred) faults (ENE trending, SE dipping) in the northern sector; (2) the San Benedetto–Gioia dei Marsi fault (SBGMF), reactivated during the 1915 Avezzano earthquake, the Parasano (PF) and the Statale Marsicana (SMF) faults in the eastern sector; (3) the Ortucchio fault (OF-inferred) near the center of the basin; and (4) the Trasacco (TF) and Luco dei Marsi (LF) faults (NW trending, SW dipping) in the southwestern sector [*Cavinato et al.*, 2002; *Galadini et al.*, 1997; *Michetti et al.*, 1996].

[21] Data from remote sensing [*Giraudi*, 1986] and subsurface investigations [*Cavinato et al.*, 2002; *Galadini and Messina*, 1994], as well as geophysical surveys (seismic, gravimetric and electrical surveys), demonstrate that a network of capable faults affect the very recent deposits of the basin floor, and outline two subbasins that are separated by a near-surface horst located along the northwestern prolongation of the Vallelonga-Trasacco ridge. The two subbasins appear to be half grabens with the main normal faults (SBGMF and TF) dipping southwest without any significant listric component (Figure 3).

[22] The cumulative vertical offset across the PF and SBGMF in the middle and late Pleistocene very likely exceeds 300 m, providing a rough slip rate on the order of 1 mm yr^{-1} [*Michetti et al.*, 1996; *Galadini et al.*, 1997]. Along the SBGMF, up to 0.9 m of vertical coseismic offset was measured after the magnitude 7.0 Avezzano earthquake of 13 January 1915 [*Ward and Valensise*, 1989; *Oddone*, 1915]. During the earthquake, typical seismogeological effects, such as liquefaction, spring anomalies, and gas and water emissions, were observed at several sites inside the plain [*Oddone*, 1915]. Furthermore, faults both bordering and cutting the basin show evidence of Holocene reactivation. Moreover, paleoseismic studies performed at several sites along the San Benedetto–Gioia dei Marsi fault (SBGMF) have demonstrated that coseismic displacement of magnitudes comparable to 1915 earthquake occurred at least once and possibly twice during the Middle Ages [*Michetti et al.*, 1996; *Galadini et al.*, 1997]. Evidence of recent activity has also been found on the Trasacco fault, which may have also been reactivated in 1915 [*Galadini et al.*, 1997]. Therefore recent and present-day activity (stronger on the eastern sector) appears to affect a network of capable fault segments distributed over the entire basin. The

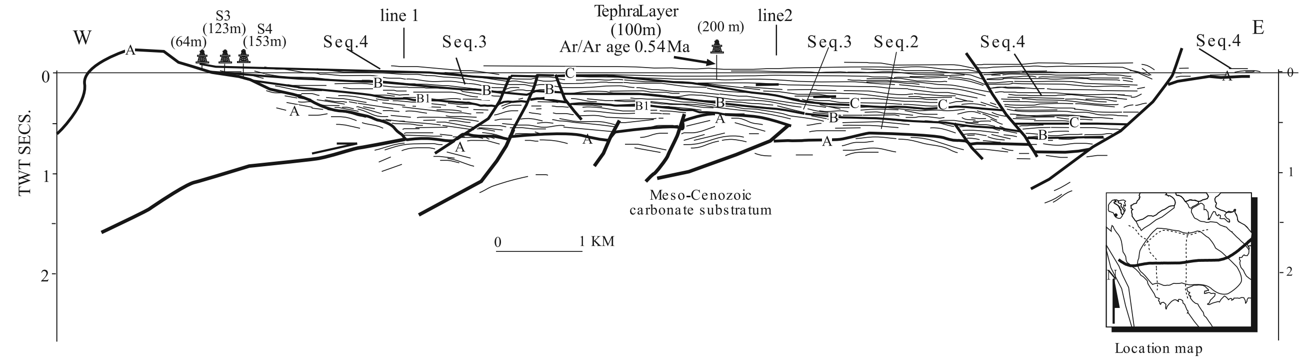

Figure 3. Seismic profile interpretation with permission of the Edison Gas, Elf, and Eni-AGIP division [after *Cavinato et al.*, 2002]. TWT, two-way traveltime.

pattern of active fault segments in the Fucino area suggests that at segment boundaries the offset is minimal and the deformation is distributed in a volume of rock instead of being concentrated on a fault plane [*Roberts et al.*, 2004, 2002; *Morewood and Roberts*, 2002].

4. Soil Gases as a Tool for Tectonic Investigations

[23] Many gas species occur in the soil air, including those originating from atmospheric, biogenic, and deep (e.g., mantle degassing, radiogenic production, rock alteration) origins. As several phenomena such as mixing and dilution, chemical and biological reactions, and differential solubility may alter the original gas concentration, a wide variation of concentrations can occur for a single species even in restricted areas. A wide suite of gases having different origins and behaviors in soils are expected to provide suitable constraints for characterizing a fracture network allowing degassing.

[24] In this work we focused our interest on the distribution of Rn, CO_2, He, and CH_4 concentrations in the soil air of a large database of samples distributed throughout the Fucino Plain. Radon is used as a tracer gas to provide a qualitative idea of gas transfer (velocity and flux), carbon dioxide is believed to act as a carrier for other gases (i.e., Rn and He), helium is used as a shallow signal of crustal leaks along faults [*Ciotoli et al.*, 2005], and methane is considered both a characteristic biogenic indicator of lacustrine deposits and a tracer of major crustal discontinuity (as supported by bursting phenomena occurred during the Avezzano earthquake [*Oddone*, 1915]).

4.1. Origin and Behavior of Gases

[25] 1. Radon (^{222}Rn) is inert, colorless, odorless, and is the heaviest rare gas occurring in nature under standard temperature and pressure conditions. With a half-life of 3.8235 days, ^{222}Rn is the only natural occurring isotope that can be used in geological, seismic and tectonic studies. The release of ^{222}Rn atoms from mineral grains to the soil pore space can result through diffusion or through a recoil effect, caused by the α decay of its parent nuclide ^{226}Ra. The ^{222}Rn diffusion coefficient in mineral grains (10^{-10}–10^{-24} m^2 s^{-1}) is quite small, so recoil is the dominant process in grains. The fraction of ^{222}Rn atoms which enters the pore space is called the emanation coefficient or emanation power [*Nazaroff and Nero*, 1988; *Tanner*, 1980; *Schroeder et al.*, 1965]. The most important influence on ^{222}Rn emanation is the ^{226}Ra concentration of the host rocks and soils, which have an average value of 40 Bq kg^{-1} [*Flexer et al.*, 1993]. In general, soils have higher emanation rates than the rocks from which they have developed, and a fine-grained soil with its large overall grain surface usually has a larger emanation rate than a coarse-grained one. Another important parameter influencing the ^{222}Rn emanation is the amount of soil moisture. Investigations by *Strong and Levins* [1982], *Stranden et al.* [1984], and *Washington and Rose* [1992] show the positive correlation between emanation coefficient and soil moisture content. There are two ^{222}Rn transport mechanisms: diffusion and advection. The diffusion coefficient (D) of ^{222}Rn in soil varies from 0.04 to 0.004 cm^2 s^{-1} [*Schroeder et al.*, 1965], but the effective diffusion coefficient (D_e) is greater due to the influence of porosity (n): $D_e = D/n$ [*Tanner*, 1980]; most soils have a coefficient on the order of 10^{-2}–10^{-3} cm^2 s^{-1} [*Nazaroff and Nero*, 1988]. During advective transport ^{222}Rn is moved passively in flowing water or soil gas (like CO_2 or CH_4). It therefore highlights not only fractures which undergo fluid circulation, but also those in which U-bearing minerals are commonly associated with clays. These characteristics allow radon to be used as a tool for the mapping of active faults in seismotectonic environments [*Toutain and Baubron*, 1999; *Ciotoli et al.*, 1998; *King et al.*, 1996; *Wang et al.*, 1991; *Hauksson and Goddard*, 1981; *Birchard and Libby*, 1978].

[26] 2. Helium (^{4}He) is a product of the uranium-thorium decay series. This rare gas is a good fracture tracer because it is chemically inert, physically stable, highly insoluble in water, and as such, it is highly mobile and able to pass through great thicknesses of fractured overburden [*Oliver et al.*, 1989, 1984; *Andrews*, 1983; *Pogorsky and Quirt*, 1981]. The concentration of helium in the atmosphere is constant (5.220 ± 0.015 ppm [*Holland and Emerson*, 1990]) as the result of the dynamic budget between degassing from the Earth and diffusion into space. Mainly generated by U-enriched rocks (1 m^3 of rock containing 1 ppm of ^{238}U produces about 1036 cm^3 of helium per million years), helium migration, as well as other gases, occurs primarily by advection from deep accumulations (geothermal fluids, uraniferous ore and hydrocarbon reservoirs) toward the surface along permeable fault and fracture systems. It is considered an exceptional marker of crustal discontinuities [*Eremeev et al.*, 1973; *Lombardi and Reimer*, 1990;

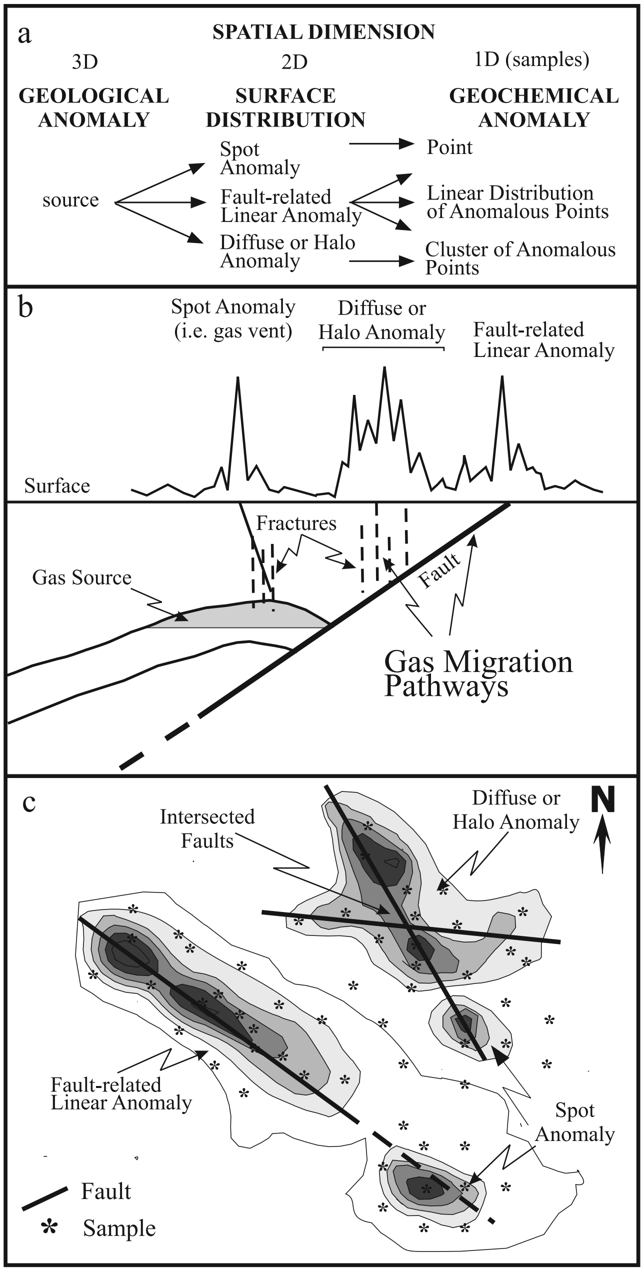

Figure 4. (a) Different types of geochemical anomalies in relation with their spatial dimension. (b and c) Section and plan view of the possible types of geochemical anomalies occurring in faulted areas [after *Ciotoli et al.*, 2005].

Duddridge et al., 1991; *Ciotoli et al.*, 1998] due to its high mobility and low reactivity.

[27] 3. Carbon dioxide is the most abundant gas species from hydrothermal to volcanic environments. The presence of carbon dioxide in fault zones may be the result of mixing of some of the following potential sources: mantle degassing, carbonate metamorphism, carbonate dissolution with subsequent CO_2 release, organic material oxidation, and microorganism or plant respiration [*Sugisaki*, 1983]. Isotopes of carbon allow one to discriminate between the different sources: $\delta^{13}C/^{12}C$ values are about 25‰, 7 to 4‰, and 0‰ for organic, mantle and sedimentary carbon, respectively [*Allard*, 1986]. Finally, one has to consider phase fractionation processes with care because CO_2 reacts with gaseous, liquid or solid constitutive components of hydrothermal systems. Dissolution of CO_2 in deep alkaline waters is a frequent feature and can lead to subsequent enrichment of poorly soluble elements such as He [*Sugisaki et al.*, 1980]. High CO_2 fluxes are often correlated with high heat flux areas (associated with active or ancient volcanism) and limited areas having deep fractures (carbon dioxide mainly originating from the mantle or crustal metamorphism). CO_2 discharges may indicate high pore pressure at depth, and therefore may serve to identify potential seismic regions [*Irwin and Barnes*, 1980]. Carbon dioxide is used for fault mapping [*Annunziatellis et al.*, 2003; *Beaubien et al.*, 2003; *Sugisaki et al.*, 1980] as well as for monitoring in both seismic and volcanic areas [*Baubron et al.*, 1991; *Shapiro et al.*, 1982].

[28] 4. Methane is a reduced form of carbon which is thought to derive from a variety of sources. Major processes involved in CH_4 genesis are microbiological (bacterial) and thermogenic, both operating on biologically formed organic matter [*Klusman*, 1993]. In active tectonic environments, methane is released close to major crustal discontinuities that show heat anomalies, and therefore is often associated with indicators of deep leaks such as He. CH_4-bearing spring gases are also known in volcanic environments (from central discontinuities to adjacent sedimentary basins).

4.2. Tectonic Signature of Soil Gas Leaks

[29] Recent works observed anomalous gas concentrations over faults and confirmed these gases as a deep fault indicators [*Baubron et al.*, 2002; *Ciotoli et al.*, 2005, 1999, 1998; *Zhang and Sanderson*, 1996; *Lombardi et al.*, 1996; *Klusman*, 1993; *Zhiguan*, 1991]. Active faults favor gas leaks because they usually increase rock and soil permeability, and thus the presence of linear soil gas anomalies longer than several meters are often taken as strong evidence of tectonic features [*Ciotoli et al.*, 1998; *Fridman*, 1990]. It is important to note that faults are typically wide fracture zones that can also be crosscut by other structures, thus resulting in diffuse or "halo" anomalies, respectively [*Matthews*, 1985; *Sokolov*, 1971]. Recent research has demonstrated that the gas-bearing properties of faults are not necessarily continuous along a tectonic structure [*Etiope et al.*, 2005; *Ciotoli et al.*, 2005; *Baubron et al.*, 2002; *Lombardi et al.*, 1996; *Ciotoli et al.*, 1998]. In these cases isolated points with high concentration values ("spotty anomalies"), are frequently observed. When multiple "spot" anomalies occur along a linear trend, one can infer that they lie along a structural feature which has a spatially discontinuous in terms of its gas conduction [*Ciotoli et al.*, 1998; *Lombardi et al.*, 1996].

[30] Extensive experience in soil gas prospecting by the authors indicates that soil gas anomalies generally occur as linear, fault linked, anomalies, as well as in irregularly shaped diffuse or halo anomalies and irregularly spaced plumes or spot anomalies [*Ciotoli et al.*, 2005, 1999; *Lombardi et al.*, 1996]. These features reflect gas migration dominated by brittle deformation both at macroscale and/or microscale. Therefore spatial patterns of soil gases in faulted areas appear to be suitable tools for identifying active

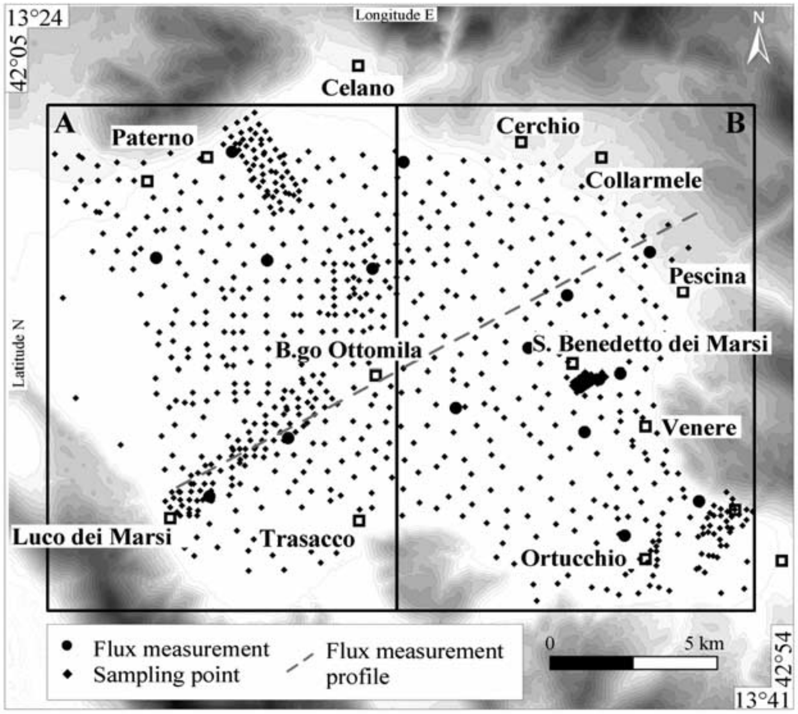

Figure 5. Location map of the soil gas samples (solid diamond) and of flux measurements (solid circles). For a better data interpretation the Fucino Plain was divided in two sectors (boxes A and B) characterized by the presence of different type (i.e., geometry) of tectonic elements. Samples collected in these two sectors have been elaborated separately by means of geostatistical techniques.

tectonic structures also in areas characterized by thick clay cover whose plastic behavior could mask the identification of faults by mean of other geological (field mapping) and geophysical methods (Figure 4).

5. Methods

5.1. Soil Gas Sampling and Analysis

[31] Soil gas surveying consists of the collection and analysis of gas samples from the unsaturated or vadose zone. In the present study samples were collected using a stainless steel probe driven into the ground to a depth between 0.7 and 1.0 m, depending on the soil consistency and thickness; this depth is considered below the major influence of meteorological variables [*Hinkle*, 1994; *Segovia et al.*,1987]. Furthermore, the collection of a large number of samples statistically minimizes sampling/analytical error and bias caused by individual samples [*Ciotoli et al.*, 2005, 1999, 1998; *Beaubien et al.*, 2003; *Annunziatellis et al.*, 2003; *Lombardi et al.*, 1996; *Hinkle*, 1994; *Reimer*, 1990].

[32] Radon is analyzed immediately in the field, due to its half-life of 3.8 days, using an EDA-200 radon active detector (Scintrex Ltd.) with a Lucas cell. A 60 mL sample, collected from the septum-capped probe via a syringe, is inserted into the radon cell (160 mL) and analyzed over a 5 min period, with counts per minute (cpm) values recorded every minute. The final 1 min value is used to calculate the ^{222}Rn, as it includes only a negligible amount of the ^{220}Rn daughters. A second 60 mL gas sample was placed in a previously evacuated, 25 mL volume, stainless-steel canister for transport and storage. Once in the laboratory, each gas sample was also analyzed for major (N_2, O_2) and minor (C_{1-4} hydrocarbon) gas species using two Fisons 8000 series packed-column gas chromatographs (GC). In addition to the GC analyses, all samples were also analyzed for helium using a Varian Portatest leak detector (model 938-41). Measurements of carbon dioxide, hydrogen sulphide and hydrogen were also made in situ by connecting the probe, via silicon tubing to a portable detector (Dräger Multiwarn II) equipped with an infrared sensor for CO_2 (0–25% v v^{-1}) and electrochemical sensors for H_2S (0–100 ppmv) and for H_2 (0–1000 ppmv).

[33] A soil gas survey was performed over the Fucino Plain (about 220 km^2) according to a regional sampling with a density of 4–6 samples km^{-2} (548 samples, Figure 5). Furthermore, three high-resolution surveys (297 samples, about 80–100 samples km^{-2}) were performed within detailed areas (transects) across the TF, ACF, and SBGMF to enhance the chances of properly recording the fault gas signal and to study fault influence on shallow soil gas distribution [*Ciotoli et al.*, 1998]. Transects were planned during the regional survey and sized (6 × 1, 3 × 1, and 0.5 × 1 km) with an average sampling density of 10–20 samples km^{-2} for transects 1 (Luco dei Marsi) and 2 (Paterno), and 80–100 samples km^{-2} for transect 3 (San Benedetto dei Marsi) in order to obtain the background gas variations in unfaulted areas as well as the fault-related anomalies. Furthermore, in order to have a semiquantitative idea of the gas leakage in the faulted and unfaulted zones, 16 measurements of soil gas exhalation (radon, carbon dioxide and methane, black circles in Figure 5) were made by using a 13 × 13 × 9 cm flux box. Measurements were made on site using the Rn detector described above and an in-house developed CO_2/CH_4 flux.

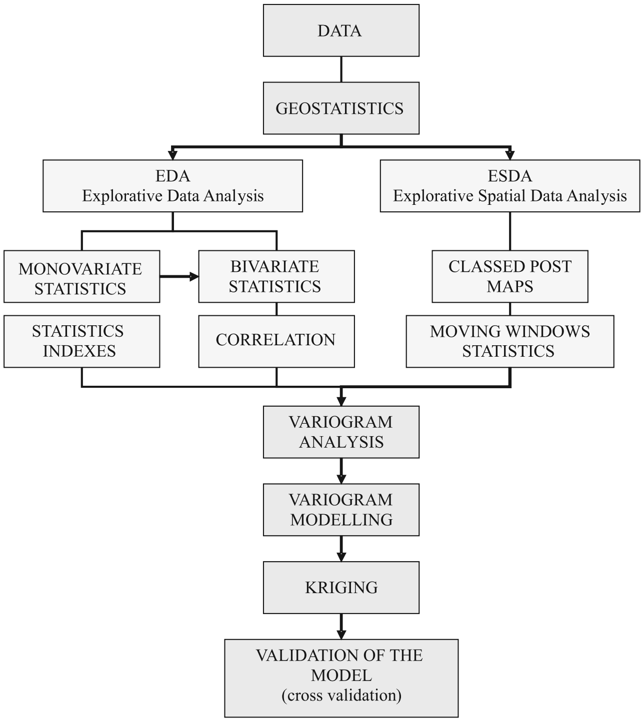

Figure 6. Flowchart of the statistical and geostatistical techniques used for soil gas data elaboration and mapping procedure.

Both soil gas sampling and exhalation measurements were accomplished in about 20 days (summer 1995).

5.2. Statistical and Geostatistical Analysis

[34] Geostatistical techniques were applied for the study of spatially correlated data, as described above. The flowchart of the general steps followed in this study is shown in Figure 6.

[35] Exploratory data analysis (EDA) was first performed to evaluate the basic characteristics of the data (i.e., summary statistics and statistical distribution of each variable). Univariate and bivariate statistical and graphical methods were used to study each variable independently, the relationship between variable pairs, as well as to highlight the presence of multiple populations, and to compare data with a large database of Italian soil gas.

[36] Exploratory spatial data analysis (ESDA) consisted of preliminary spatial data representation by using classed-post maps to show value distribution and to visualize the intersample distance, which is useful to determine the grouping intervals for experimental semivariogram calculation and to choose search radii in estimation routines (kriging).

[37] Variogram analysis is performed to check spatial continuity of the data values and the presence of anisotropies. Once spatial continuity is characterized it is modeled with variogram functions that form the basis for kriging estimation. Finally, cross validation was used to validate the model parameters used for the estimation.

[38] Collected data were computer processed by using the following software: Statistica 6.0 (StatSoft, Inc.), GS+, Geostatistical Software for Environmental Science (Gamma Design Software, LLC) and Surfer 8 (Surface Mapping System, Golden Software, Inc,).

6. Results

6.1. Exploratory Data Analysis

[39] The exploratory data analysis (EDA) shows that Rn, CO_2, N_2 and O_2 have low dispersed distributions, as highlighted by the low value of the coefficient of variation (CV) (Table 1). Otherwise, the wide ranges, as well as the high skewness values, for CH_4 and He indicate the presence of outliers. The mean and median values for CH_4 (14.03 ppm and 1.12 ppm) and He (5.33 ppm and 5.28 ppm) highlight that the frequency distribution of these gases are positively skewed (18.99 and 9.34, respectively), indicating an exponential or lognormal distribution. In the case of skewed distributions, the median and the interquartile range (IQR) (1.12 and 1.18 for CH_4 and 5.28 and 0.17 ppm for He), are better than the mean and the standard deviation to provide data dispersion and to highlight values that may be considered anomalous. Results of the Kolmogorov-Smirnov test ($p < 0.01$) confirms a nonnormal distribution for all variables, and as geostatistical analysis provides poor results with nonnormal sample distributions, the data have been log transformed to improve the fit with a normal distribution.

[40] In this study a comparison with a large soil gas database collected in Italy by the authors since 1975 has been performed in order to validate the Fucino data set in terms of bias errors (sampling and analysis), as well as of the detection of a possible anomaly cutoff. Table 2 shows the main statistical parameters for radon for both this study and the complete Italian database, as well as a subset of data collected in other intermontane basins. Box plot are used to display and compare the distribution of the Fucino data set

Table 1. Main Statistics of Soil Gas Data[a]

	Samples	Mean	Median	Min	Max	Lower Quartile	Upper Quartile	IQR	SD	Skewness
Rn, kBq m^{-3}	845	19.40	14.80	0.00	119.51	7.40	27.01	19.61	16.76	1.60
CO_2,%	845	3.35	2.64	0.02	20.54	1.24	4.36	3.12	3.11	2.18
CH_4, ppm	844	14.03	1.12	0.01	3913.50	0.69	1.87	1.18	168.96	18.99
He, ppm	845	5.33	5.28	4.33	13.46	5.20	5.37	0.17	0.50	9.34
N_2,%	586	76.69	77.41	60.64	81.35	76.47	78.18	1.71	2.81	−3.11
O_2,%	586	18.61	18.78	9.20	23.53	17.64	20.00	2.36	2.06	−0.98

[a]The main statistics of soil gas data show that Rn, CO_2, N_2, and O_2 have low dispersed distributions as highlighted by the low value of the standard deviation. Otherwise, the wide ranges, as well as the high values of the skewness, for CH_4 and He concentrations indicate the presence of outliers. The mean and the median values for CH_4 and He highlight that the frequency distribution of these gases are positively skewed, indicating an exponential or lognormal distribution of these variables. In the case of skewed distributions, the median and the interquartile range (IQR) of CH_4, and of He, are better than the mean and the standard deviation to provide data dispersion and to highlight values that may be considered as anomalous.

Table 2. Main Statistical Parameters of Radon Data Collected in Different Geological Scenarios[a]

	Samples	Mean	Median	Min	Max	Lower Quartile	Upper Quartile	SD	Skewness
1, Fucino	794	20.50	15.50	0.37	120.00	8.50	28.00	16.80	1.60
2, South Vittorino	379	20.80	11.50	0.10	599.80	6.70	22.00	40.20	9.80
3, Tagliacozzo	196	84.90	58.80	0.37	519.90	22.00	129.00	83.60	1.80
4, Val Roveto	100	29.90	24.80	3.33	112.50	19.20	33.00	19.20	2.00
5, Val Comino	491	72.40	48.50	1.11	483.20	27.00	87.00	71.80	2.50
Intermontane basins	2890	32.70	17.70	0.10	599.80	8.90	36.00	48.20	4.40
Neogenic basins	717	15.40	7.80	0.37	121.40	3.00	21.00	18.20	1.90
Foredeep basins	2359	19.10	12.90	0.37	241.20	3.10	26.00	22.90	3.20
Volcanic areas	3664	47.60	31.82	0.00	480.26	14.06	63.64	49.82	2.39

[a]Comparison among soil gas radon values measured in different intermontane basins, with those measured in neogenic and foredeep and volcanic areas in Italy. Numbers in the location column correspond with the numbers in Figure 1.

with those collected in different geological scenarios in Italy (volcanic areas, neogenic basins, foredeep basins, intermontane basins, mining areas) (Figure 7). The graphs indicate that (1) the median value of radon activity (14.80 kBq m^{-3}) is comparable with that calculated for other intermontane basins in Italy (17.70 kBq m^{-3}), which is the highest compared with the other studied geological scenarios (excluding the value 45.81 kBq m^{-3} for volcanic areas, highlighting the influence of active tectonic structures); (2) the median value of CO_2 (1.93%) is the highest among the considered geological scenarios (the median value of the entire CO_2 database, about 11000 data, is 0.81%); and (3) the median values of CH_4 (1.09 ppm) and He (5.24 ppm) are the lowest among the considered areas.

[41] These preliminary considerations indicate that active gas-bearing faults present in the seismic intermontane basins favor gas leakage. In particular, the high median values of Rn and CO_2 confirm the presence of high gas microseeps, as well as the known behavior of carbon dioxide acting as carrier for trace gases (i.e., radon). The low median values of He and CH_4 concentrations could be due to dilution by major atmospheric components, i.e., nitrogen, oxygen, and carbon dioxide. Furthermore, dilution by surface gases of biological origin may also alter CO_2 and CH_4 signatures. In this case the

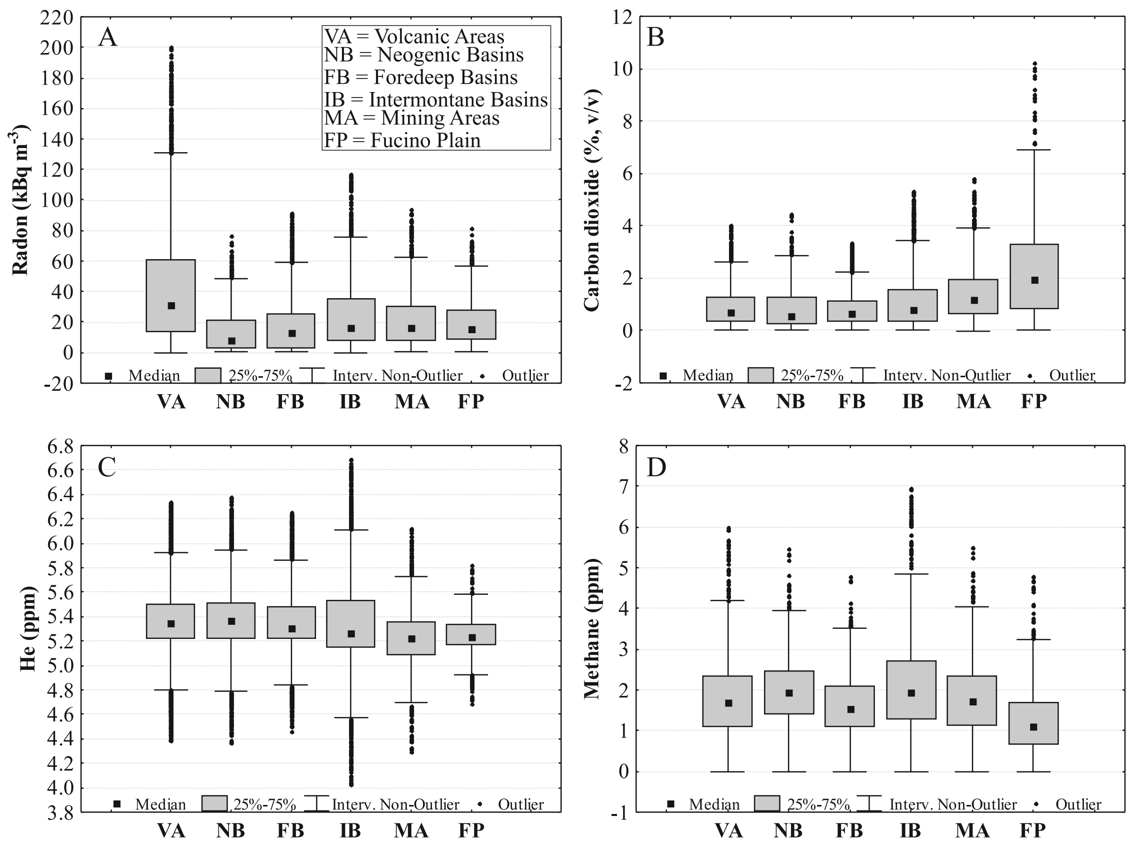

Figure 7. Box plots show the comparison between the concentration of different soil gas species in different geological settings on the basis of more than 20,000 samples collected in central Italy since 1975. Plot highlights that radon concentrations measured in the Fucino Plain (FP) show the highest median value, excluding the volcanic areas (VA) where high radon values are linked to the high radium content (Figure 7a). Carbon dioxide concentrations also shows the highest values mainly linked to gas migration along the main faults (Figure 7b).

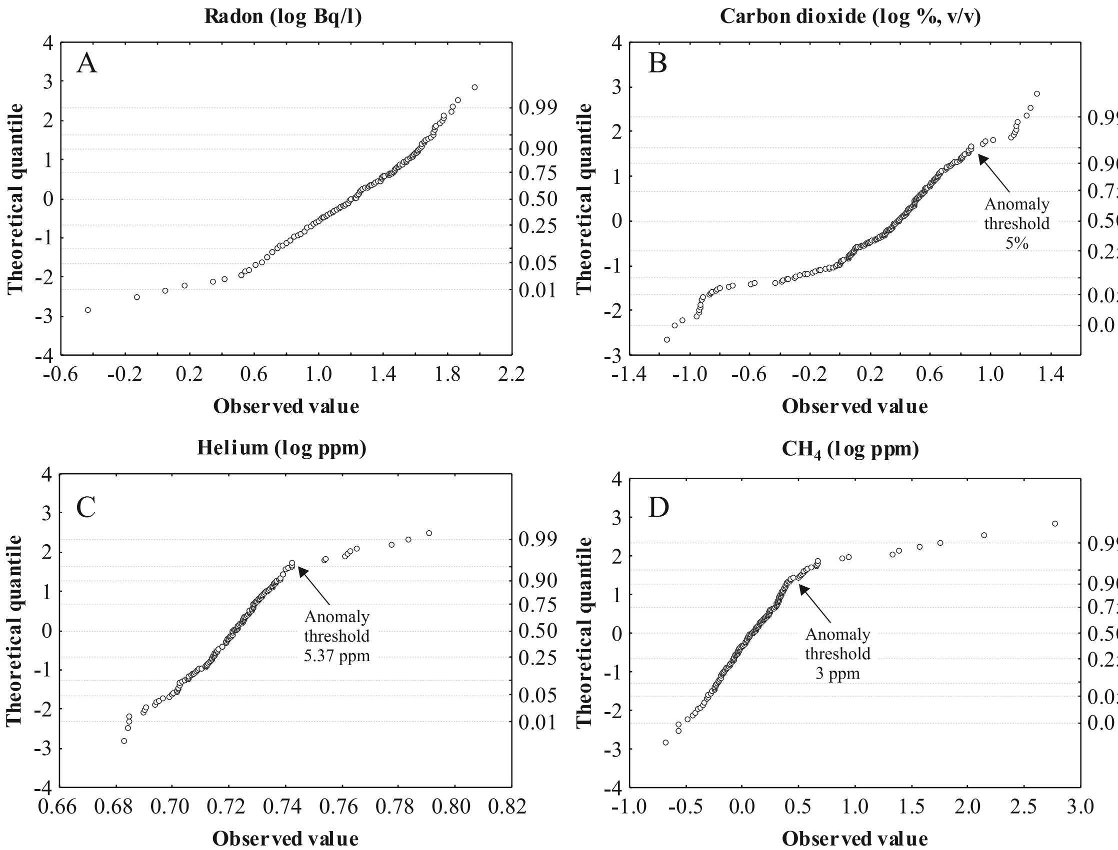

Figure 8. Quantile-quantile plots (Q-Q plot) calculated for trace (He and Rn) and minor gases (CO_2 and CH_4). Plots highlights anomaly threshold values of 5% for CO_2 (Figure 8b), 5.37 ppm for He (Figure 8c), and 3 ppm for CH_4 (Figure 8d). The Q-Q plot of logarithmic transformed Rn data shows a linear distribution of the points (Rn has a lognormal distribution), so it is not possible to highlight a well defined threshold of anomaly.

shallow distribution of fault-related anomalies of these minor and trace species can be shown by spot values that could show a linear pattern. These soil gas anomalies, however, may display a complex character, both in space and time. For example, anomalies may differ according to the structure of the faults, such as fault gouges versus intensely sheared zones, resulting in a different shallow pattern due to the low gas permeability of fault gouge materials compared to high permeability of fractured rocks in the adjacent shear zones [*Ciotoli et al.*, 2005; *King et al.*, 1996; *Sugisaki et al.*, 1980]. On this basis gas anomalies in correspondence of active faults can be either "direct leak anomalies" indicating a deep gas origin, or "secondary anomalies" linked to the shallower chemical-physical nature of the fault-constituting rocks.

[42] Because soil gases have a different abundance with respect to the atmospheric air, (0.01 kBq m^{-3} for ^{222}Rn, 0.036 for CO_2, 1.4 ppm for CH_4, 5.20 ppm for He, 78.08% for N_2% and 19.4% for O_2), the detection of an anomaly threshold constitutes a fundamental step in the exploratory statistical analysis for further discussion about the possible sources of the studied gases. Various statistical methods can be applied to assess the anomalies relative to background [*Ciotoli et al.*, 2005; *Beaubien et al.*, 2003; *Sinclair*, 1991]. In general, our experience, based on the collection and analysis of more than 30,000 soil gas samples in different geological scenarios, highlights a strong correspondence between the upper quartile and the anomaly threshold. In should be remembered, however, that soil gas anomalies cannot be fixed absolutely, but rather must be defined locally due to their complex origins.

[43] According to *Sinclair* [1991] the normal probability plot (NPP) or the quantile-quantile plot (Q-Q plot) provides a good method to distinguish different, often overlapping, populations (i.e., background, anomalous values, and outliers) and a more objective approach to statistical anomaly threshold estimation (Figure 8). Figure 8 highlights the anomaly threshold values for He (5.37 ppm) CO_2 (5%) and CH_4 (3 ppm). The NPP of logarithmically transformed Rn data shows a linear distribution of the points, so it is not possible to define a clear anomaly threshold. In this case the radon anomaly cutoff was calculated using the ^{222}Rn activity at equilibrium with parent radionuclides (^{226}Ra) in collected soil samples [*Ciotoli et al.*, 1998], using the Akerblom formula [*Åkerblom*, 1993]

$$C_{Rn} = C_{Ra} \varepsilon \rho \ n^{-1} \qquad (2)$$

where C_{Rn} and C_{Ra} are radon in soil gas (Bq L^{-1}) and radium in soil (Bq kg^{-1}), respectively, and, ε is the emanation power coefficient (dimensionless), ρ is soil density (kg L^{-1}), and n is the effective porosity coefficient

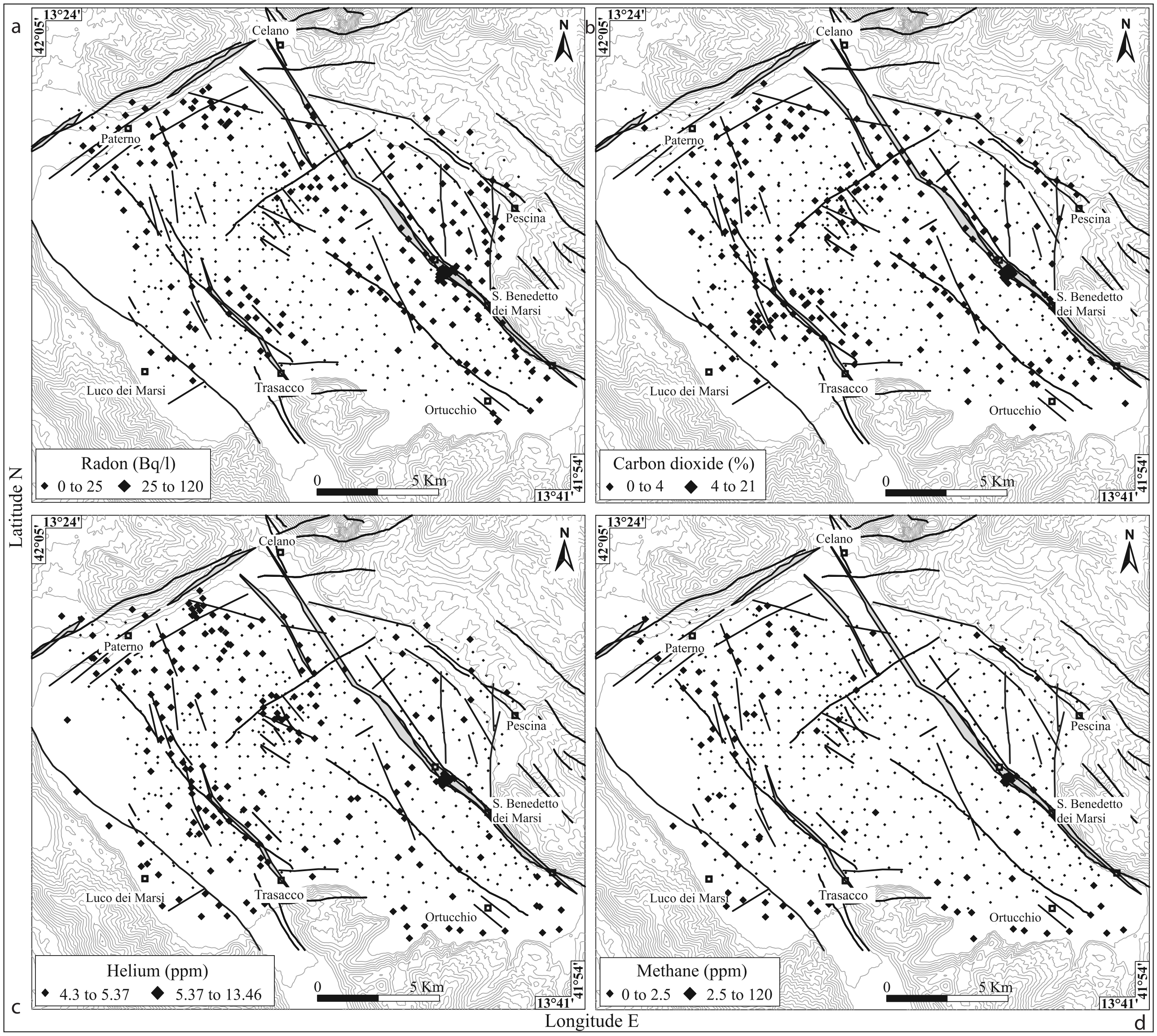

Figure 9. Classed post maps show that (a) radon and (b) carbon dioxide anomalous values highlight the shallow scarps of the seismogenic and recently activated normal faults in the eastern sector (i.e., SBGMF, OF), as well as the buried structural elements in the western sector (i.e., the southern part of the TF, ACF). Highest (c) helium and (d) methane values prevail in the western side of the studied area along the TF, ACF, LF. Helium distribution locally also corresponds the ACF in the northwestern sector of the plain and with a wide anomalous zone located in the central part of the plain where liquefaction-induced deformations occur.

(nondimensional). Assuming $\varepsilon = 0.2$ typical of fine-grained soil, $n = 0.3$, as suggested by geotechnical studies in the Bacinetto area [*Burghignoli et al.*, 1991] and substituting the measured mean Ra activity sample densities, the formula yields a mean value of 26.41 kBq m^{-3} of radon at equilibrium with its parent nuclide. This value can be considered as the anomaly threshold, and thus radon concentrations greater than this can be linked to an upward migration along enhanced permeability pathways (i.e., faults).

6.2. Exploratory Spatial Data Analysis

[44] The basic elements of ESDA include data visualization using postplots (classed-post), or indicator postplots to study spatial patterns.

[45] The radon distribution in the Fucino Plain is different for faults bordering versus those cutting the Fucino Plain (Figures 9a, 9b, 9c, and 9d). This difference likely originates from tectonic features such as geometry (high angle, listric faults), seismic activity (seismogenic faults or coseismic fractures), and depth (blind faults). Anomalous radon values strike along the shallow scarps of the seismogenic and recently activated normal faults in the eastern sector (i.e., SBGMF, OF, the N-S fault recognized by *Oddone* [1915] near the village of Pescina). Otherwise, they mark NW-SE trending belts of enhanced permeability, located along buried structural elements which are known or inferred on the basis of structural interpretation of field or

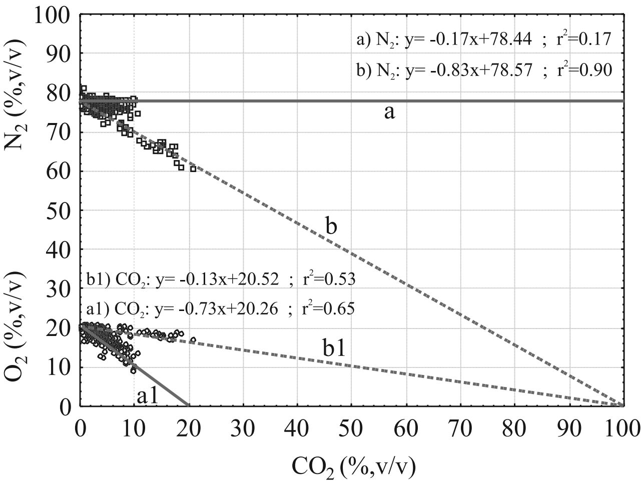

Figure 10. The scatterplot of CO_2 versus N_2-O_2 shows the presence of two populations of samples: (1) an in situ consumption of O_2 (e.g., chemical and/or biological reactions) shown by the stoichiometric 1:1 decrease in oxygen (a and a_1 solid lines) and (2) an inverse relationship between CO_2 versus both N_2 and O_2 caused by a dilution of these two major species implying a deep input of carbon dioxide (b and b_1 dotted lines).

subsurface data, in the western sector (i.e., the southern part of the TF, ACF).

[46] Anomalous carbon dioxide values agree well with the shallow radon activity highlighting a strong fit with the fault systems of the Fucino basin (Figure 9b). This strong correlation supports the presence of buried gas-bearing channels in the plain where the migration of CO_2 acts as carrier for trace species, suggesting a potential deep origin of these gases. This hypothesis is strengthened where methane and helium anomalies are also measured (particularly in the western sector). Furthermore, a scatterplot of CO_2 versus N_2-O_2 (Figure 10) shows the presence of two populations of samples: (1) an in situ consumption of O_2 (e.g., chemical and/or biological reactions) shown by the stoichiometric 1:1 decrease in oxygen; and (2) an inverse relationship between both N_2 and O_2 versus CO_2, caused by the dilution of the first two by the latter and implying the upward flux of deep carbon dioxide. However, to reinforce the hypothesis about the origin of CO_2, carbon isotopic analyses are required.

[47] Highest helium values prevail on the western side of the studied area along the TF, ACF, an LF (Figure 9c), appearing to characterize a fracturing zone linked to the buried carbonate structural high located on the northwestern prolongation of the Vallelonga-Trasacco ridge (see Figure 3). It is possible that the pervasive fracturing of this relatively shallow structure enhances helium leakage from a deeper source. Furthermore, most of the CO_2 values above 4% agree with the highest helium concentrations (above 5.37 ppmv), suggesting that the TF and ACF could be preferential pathways for the ascent of CO_2 enriched in a component coming from carbonate dissolution. Helium distribution also corresponds locally with coseismic ruptures that intersect the ACF in the northwestern sector of the plain, and with a wide anomalous zone located in the central part of the plain where liquefaction-induced deformations occur. In the eastern sector of the plain high He values occur close to the OF, but slightly displaced toward west with respect to the Rn anomalous samples.

[48] The interpretation of CH_4 data is generally complex because this gas can be biologically produced in an-oxic lacustrine sediments which are commonly rich in organic matter but can be biologically consumed in oxic soils. Figure 9d shows that anomalous samples are located mostly in the western side of the plain in correspondence with the ACF and LF. The origin of methane can be interpreted based on isotopic signatures ($\delta^{13}C$ and associations with other gases (e.g., heavier hydrocarbons).

[49] The high sampling density used in the detailed surveys carried out across the main fault systems highlight that a sampling scale effect could affect the observed soil gas distribution, as they show slightly higher values than the local background (see Figure 5). In particular, it is worth noting that almost all the samples collected within the transect crossing the SBMF show anomalous gas concentrations: up to 92 kBq m^{-3} of radon, 2520 ppm of methane, 17.2% of carbon dioxide, and 6.2 ppm of helium. At high-resolution scale this behavior, linked to the different contribution of phenomena acting along specific directions (i.e., fault-related anisotropy) versus those acting randomly (i.e., isotropic field of background), is less apparent than at the regional scale. This may originate because of a "scale effect," when sampling is performed within the influence "domain" (spatial range) of a structure (e.g., a fault). Nevertheless, channeling phenomena, because of their very close spatial influence, can also be clearly seen by high-resolution surveys. Coupled regional and high-resolution sampling provides information about the spatial influence of the structural features on the soil gas data. Variogram elaboration and analysis can greatly enhance the sampling strategy (see section 6.3).

[50] Among the ESDA techniques, moving window statistics is used for spatial trend visualization and variable stationarity assessment. A regular grid (3 $\times$ 3 km) was applied over the data, and several local statistics, such as mean or median and standard deviation, were calculated in each grid cell and their spatial variation was studied over the area; cells containing less than 4 measurements were discarded. In general, the mean and the standard deviation of a lognormal distribution are not independent of one another. The consequence is that when different sample sets are taken from the same lognormal distribution the standard deviation of the samples is directly proportional to their mean. As an example of this technique the results obtained by a moving window statistics of radon values are shown in the classed post map and in the scatterplot of Figures 11a, 11b, and 11c. Figure 11 highlights the following features: (1) constant low and high mean radon levels in the western and eastern sector of the plain, respectively (Figure 11a); (2) a slightly increasing NE trend; and (3) a clear linear relationship between local mean radon levels and standard deviations (R^2 = 0.86), pointing out the presence of a strong proportional effect that implies heteroscedasticity of raw data, i.e., the variability depends on the mean value (Figure 11c).

[51] This analysis gives a first impression about the spatial distribution of soil gas data, suggesting stationarity

for radon levels in the western and eastern sectors of the plain. Stationarity or quasi-stationarity of the variable are required to perform a variogram analysis and modeling.

[52] Exhalation measurements show mean flux values of Rn, CH_4 and CO_2 comparable with those measured in faulted and unfaulted zones of other tectonic basins of the central Italy (i.e., Siena basin, Table 2). In particular, the highest fluxes were measured in correspondence of the recently activated faults of the eastern sector (i.e., SBGMF and OF), and the similar behavior of Rn and CH_4 provides a further proof of carrier action of methane (and subordinately CO_2) versus radon (Figure 12).

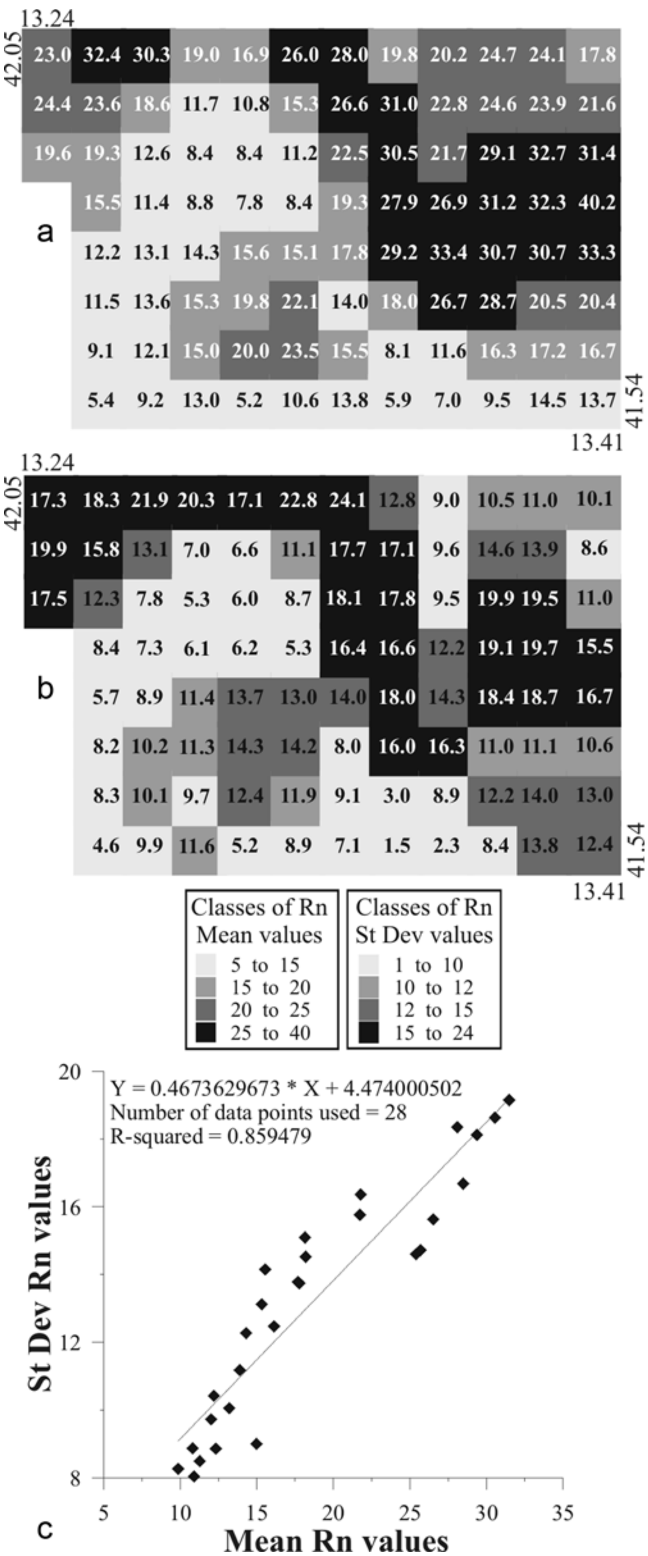

Figure 11. Results obtained by a moving windows statistics of radon values shown (a and b) in the classed post maps and (c) in the scatterplot. The following are highlighted: (1) a constant low and high mean radon levels in the western and eastern sector of the plain (Figure 11a); (2) a slightly increasing NE trend; and (3) a clear linear relationship between local mean radon levels and standard deviations (R^2 = 0.86), pointing out the presence of a strong proportional effect (i.e., the variability depends on the mean value, Figure 11c). This analysis suggests a stationarity for radon levels in the western and eastern sectors of the plain.

6.3. Geostatistical Analysis

[53] The difficulty of variogram analysis, or "variography," depends on the quality and quantity of data and on the complexity of the studied phenomenon. Variography is a stepwise process, since the user will decide what variogram models will be fitted, thus influencing the interpolation which will be done using the kriging method.

[54] In linear geostatistics, as in conventional statistics, a normal distribution for the variable under study is desirable. Even though normality may not be strictly required, high skewness and outliers can impair the variogram structure and the kriging results. For this reason, the variographic study was performed only for CO_2 and Rn, both because they constitute a typical carrier/trace gas association and because they show a less skewed data distribution than He and CH_4. Furthermore, as CO_2 and Rn have generally a lognormal distribution, data was log transformed in order to reduce the influence of outliers [*Annunziatellis et al.*, 2003; *Beaubien et al.*, 2003; *Astorri et al.*, 2002].

[55] Preliminary ESDA (dot maps) highlights that radon can be considered as a stationary variable within the two separate sectors. In order to study the different contribution of direction-specific versus random phenomena a geostatistical analysis was performed using Rn and CO_2 subsets collected in the two sectors of the plain (dashed rectangles in Figure 5). If experimental variograms are constructed on different sets of samples within an area, the proportional effect can have a radical effect on the appearance of the variograms, especially in the construction of experimental variograms in different directions when studying anisotropy. In this case directional variograms can differ in total sill value, highlighting a false "zonal anisotropy." For this reason it is recommended to remove the proportional effect by calculating "relative variograms," where each pair difference is divided by the average of the individual pair of samples. The relative variogram is analogous to the variogram calculated using the logarithmic of the sample values. Logarithmic variograms were calculated here since this calculation is simpler and because the calculation of "semivariance" becomes more sensitive and stable. The average distance between samples (about 650m) was used as the lag distance (x axis of the experimental variogram graphs) to calculate the γ difference between sample pairs.

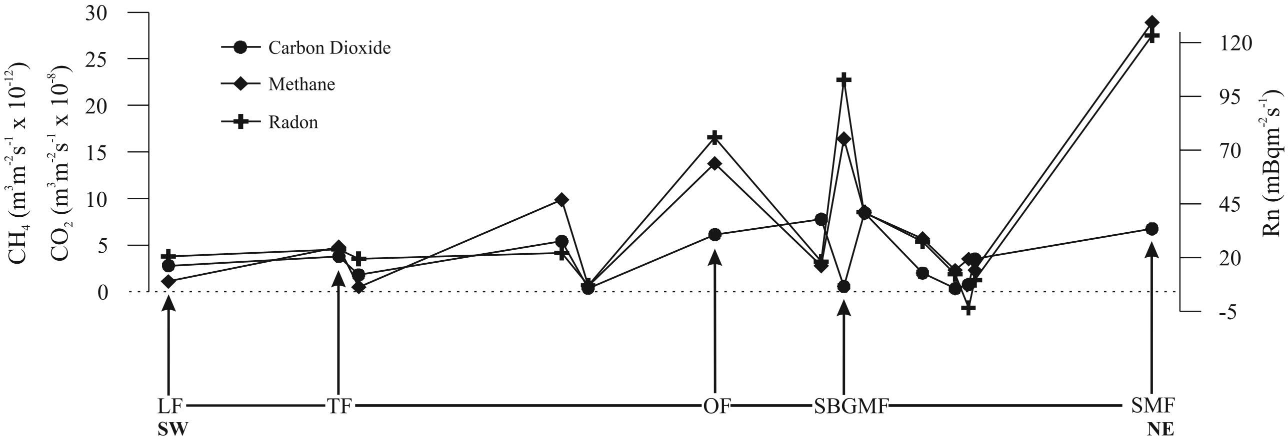

Figure 12. Exhalation measurements show mean flux values of Rn, CH_4, and CO_2 comparable with those measured in faulted and unfaulted zones of other tectonic basins of the central Italy (i.e., Siena basin, Table 2). Figure highlights that highest fluxes were measured in correspondence of the recently activated faults of the eastern sector (i.e., SBGMF and OF), and a similar behavior of Rn and CH_4. This fact provides a further proof of carrier action of the methane (and CO_2) versus radon.

[56] Figure 13 shows the variogram surface maps for carbon dioxide and radon, as well as the modeled experimental variograms for the eastern sector calculated along different orientations. The various orientations are presented to visualize anisotropies, thereby improving the choice of orientations along which to calculate the directional variograms. The elongated shapes highlighted by the lower γ values (dark gray-toned squares) in the variogram maps (Figure 13) indicate an anisotropic distribution, as well as the presence of a spatial correlation domain. The axes of the ellipse show the directions and ranges (i.e., distances in field units) of the minimum and maximum axes of anisotropy. The variogram maps stress the following features:

[57] 1. Minimum γ values occur along the maximum anisotropy axis (145° for CO_2 and 130° for Rn. Note that in variogram analysis, angles are measured counter clockwise the trigonometric 0 angle, i.e., east), correspond to the direction of maximum data continuity, and in agreement with the Apennine direction of the recognized faults in the sector.

[58] 2. Maximum γ values along the direction of the minimum axis of anisotropy (55° for CO_2 and 45° for Rn) correspond to the direction of high spatial data variability, orthogonal to the direction of the main faults.

[59] 3. The anisotropy ratio (R), given by the relation A_{max}/A_{min} (where A_{max} and A_{min} are the lengths of the maximum and minimum anisotropy semiaxes, i.e., the ranges of the experimental variograms), has a value of $R \cong 5$ for both gases, suggesting the effective influence of anisotropy-inducing factors (fault-linked) and a quantitative measure of the distance along which the fault influences shallow CO_2 and Rn distributions.

[60] The experimental variograms of CO_2 and Rn for the eastern sector were calculated along the maximum and minimum anisotropy axes (Figures 13a and 3b); they confirm the presence of anisotropy as they reach the same sill value at different ranges. In particular, the CO_2 experimental variogram calculated along the maximum anisotropy direction (145°) shows a maximum range value of 5.5 km, while the experimental variogram calculated in the orthogonal direction (55°) shows the minimum range value of 1.6 km. Rn experimental variograms also show similar ranges of 6 and 1.2 km along the maximum (135°) and minimum (45°) anisotropy directions, respectively. It is worth noting that the orientation of the maximum anisotropy axis fits well with the orientation of the OF and SBGMF (N315) occurring in the eastern sector of the plain. Furthermore, the short range in the directional variogram (calculated orthogonal to the main anisotropy) explains the high gas concentrations measured in the detailed sampling (about 1 km long) across the SBGMF, and confirms that all transect samples were collected in the spatial domain of the fault along the minor anisotropy axis.

[61] The CO_2 and Rn experimental variograms for the eastern sector were then modeled along the maximum anisotropy direction (145° and 135°, respectively). Two selected spherical models have the following equations: $\gamma(h) = 0.07 + 0.015$ Sph. (5.5) for carbon dioxide (Figure 13a) and $\gamma(h) = 0.04 + 0.06$ Sph (6) for radon (Figure 13b).

Figure 13. Variogram surface maps of carbon dioxide and radon data, as well as modeled experimental variograms calculated for data collected in the (a, b) eastern and (c, d) western sectors of the Fucino Plain. The variogram maps highlight maximum axes of anisotropy oriented 145° for CO_2 and 135° for Rn in the eastern sector and 135° for CO_2 and 135° for Rn in the western sector. These directions are in agreement with the Apennine direction of the recognized faults. Experimental variograms calculated for the eastern sector (Figures 13a and 13b) are modeled by using a simple spherical model (bold line), whereas experimental variograms calculated using CO_2 and Rn data collected in the western sector (Figures 13c and 13d) show are modeled by using nested models (e.g., two spherical models; bold line). The parameters of the model equations will be used in the kriging algorithm to calculate contour maps.

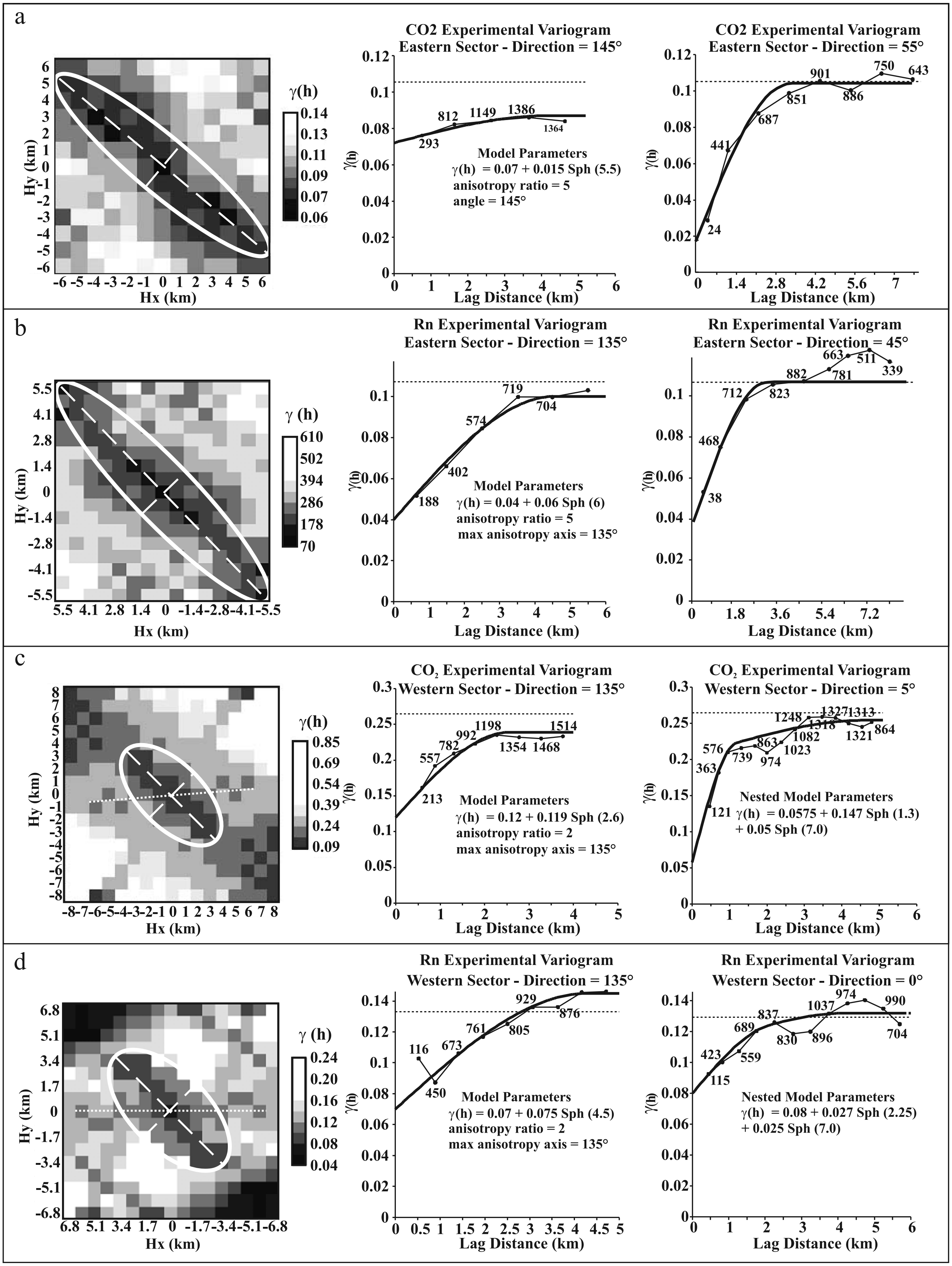
a
CO2 Experimental Variogram
Eastern Sector - Direction = 145°
Model Parameters
γ(h) = 0.07 + 0.015 Sph (5.5)
anisotropy ratio = 5
angle = 145°
CO2 Experimental Variogram
Eastern Sector - Direction = 55°
b
Rn Experimental Variogram
Eastern Sector - Direction = 135°
Model Parameters
γ(h) = 0.04 + 0.06 Sph (6)
anisotropy ratio = 5
max anisotropy axis = 135°
Rn Experimental Variogram
Eastern Sector - Direction = 45°
c
CO2 Experimental Variogram
Western Sector - Direction = 135°
Model Parameters
γ(h) = 0.12 + 0.119 Sph (2.6)
anisotropy ratio = 2
max anisotropy axis = 135°
CO2 Experimental Variogram
Western Sector - Direction = 5°
Nested Model Parameters
γ(h) = 0.0575 + 0.147 Sph (1.3)
+ 0.05 Sph (7.0)
d
Rn Experimental Variogram
Western Sector - Direction = 135°
Model Parameters
γ(h) = 0.07 + 0.075 Sph (4.5)
anisotropy ratio = 2
max anisotropy axis = 135°
Rn Experimental Variogram
Western Sector - Direction = 0°
Nested Model Parameters
γ(h) = 0.08 + 0.027 Sph (2.25)
+ 0.025 Sph (7.0)
Hx (km)
Hy (km)
γ(h)
Lag Distance (km)

Figure 13

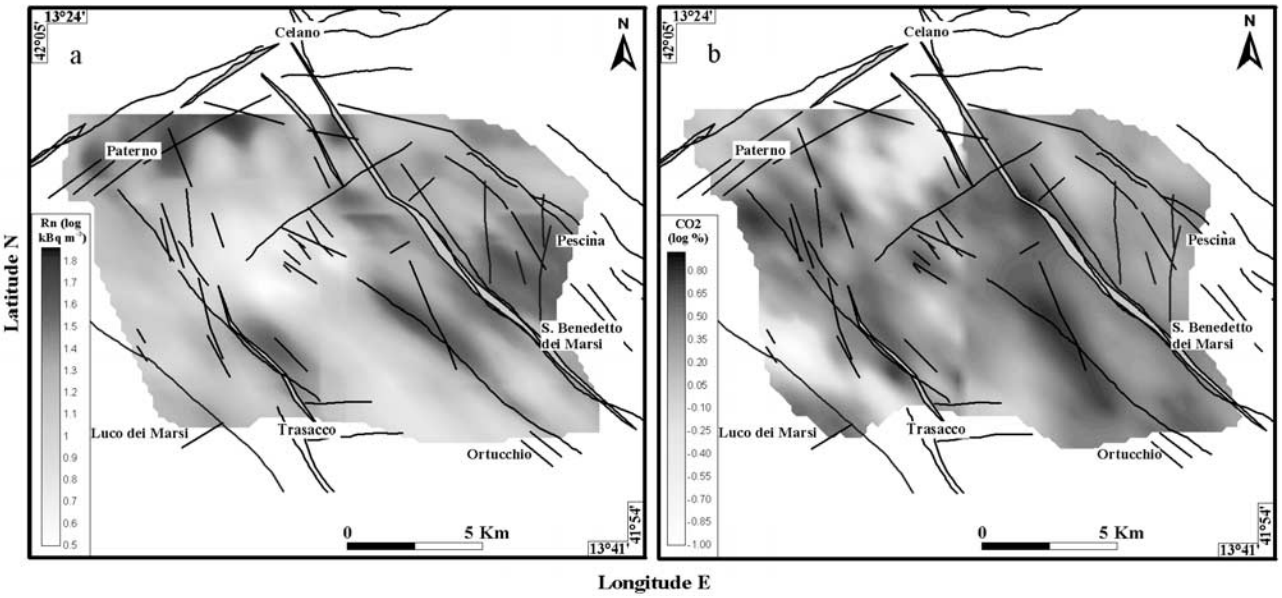

Figure 14. Contour maps of (a) Rn and (b) CO_2 in the Fucino Plain. Radon and carbon dioxide anomalies well fit with the trend of known structural features both in the eastern and western sectors. Higher Rn levels and CO_2 concentrations characterize the eastern sector of the Fucino Plain where the most active/recently activated faults (OF and SBGMF) occur. In the western sector, radon distribution defines the southern and the northern segments of the known Trasacco Fault (TF) in agreement with the structural observations. The lateral diffusion of the anomalies in the area of the TF confirms the rotation of the anisotropy axis toward the E-W direction probably due to the presence of a more complex fault geometry (wide fracturing).

[62] The fitted models consist of a nugget value (0.07 and 0.04) and a spherical function (*Sph*), for which at distances greater than range values (5.5 and 6) pairs of points will no longer be autocorrelated and thus the semivariogram reaches the asymptotic sill value $\gamma = C_0 + C$. For example, the sill value of the radon variogram model consists of a nugget variance ($C_0 = 0.04$) and a structural variance (C = 0.06) ($\gamma = 0.04 + 0.06 = 0.1$).

[63] The CO_2 and Rn variogram maps for the western sector highlight a quite different spatial domain (Figure 13). They stress the following features: (1) a maximum anisotropy axis (135° for CO_2 and Rn, Figures 13c and 13d) which corresponds to the direction of maximum data continuity, and in agreement with the Apennine direction of the recognized TF in the sector; (2) a minimum anisotropy axis (55° for CO_2 and Rn) which corresponds to the direction of high spatial data variability, orthogonal to the direction of the main fault; (3) further anisotropies (dotted line) along directions 5° for CO_2 and 0° for Rn; and (4) the anisotropy ratio (R) is 2 for both gases, suggesting that in this sector the anisotropy-inducing factors (fault-linked) produce a reduced spatial continuity for both shallow CO_2 and Rn.

[64] In fact, the experimental variograms calculated using CO_2 and Rn data from the western sector of the plain show a more complex structure. The experimental variograms of both gases calculated along the 135° (N315) direction show a simple structure, suggesting also for this sector of the plain the presence of an anisotropic phenomenon linked to the Apenninic fault system (TF). In contrast the experimental variograms calculated along the E-W direction shows two sills (domain of spatial influence) at different ranges of 1.2 and 7 km for CO_2 data and 2.25 and 7 km for Rn data.

[65] The computed experimental variograms were studied using simple models along the maximum anisotropy axis (135°) and nested models along the E-W direction (Figure 13c). The model equations of CO_2 experimental variograms are $\gamma(h) = 0.12 + 0.119$ Sph. (2.6) and $\gamma(h) = 0.0575 + 0.147$ Sph. (1.3) + 0.05 Sph. (7). The model equations of Rn experimental variograms are $\gamma(h) = 0.07 + 0.075$ Sph. (4.5) and $\gamma(h) = 0.08 + 0.27$ Sph. (2.25) + 0.025 Sph. (7) (Figure 13d). These variograms highlight that shallow gas distribution in the E-W direction shows a spatial continuity linked to phenomena acting at two scales: a minor (local) scale up to about 2 km and a major (regional) scale up to about 7 km.

[66] The parameters of the fitting models are used in the kriging algorithm calculations to predict (interpolate/extrapolate) "observation" values at unsampled locations within the area of interest. The prediction makes use of the spatial dependencies of the measurement values of the input data provided by the variograms.

[67] Figures 14a and 14b show the contoured radon and carbon dioxide values in the Fucino Plain using the parameters of the selected variogram models. The cross validation technique is used to provide the goodness of fit of the selected models at unsampled locations. Cross validation removes a known sample value at a given location and estimates its value by using the selected parameters of the variogram models and the surrounding values. This procedure follows for all known samples, thereby calculating the biases of the estimation algorithm. Figure 15 shows an example of the cross-validation technique used to validate

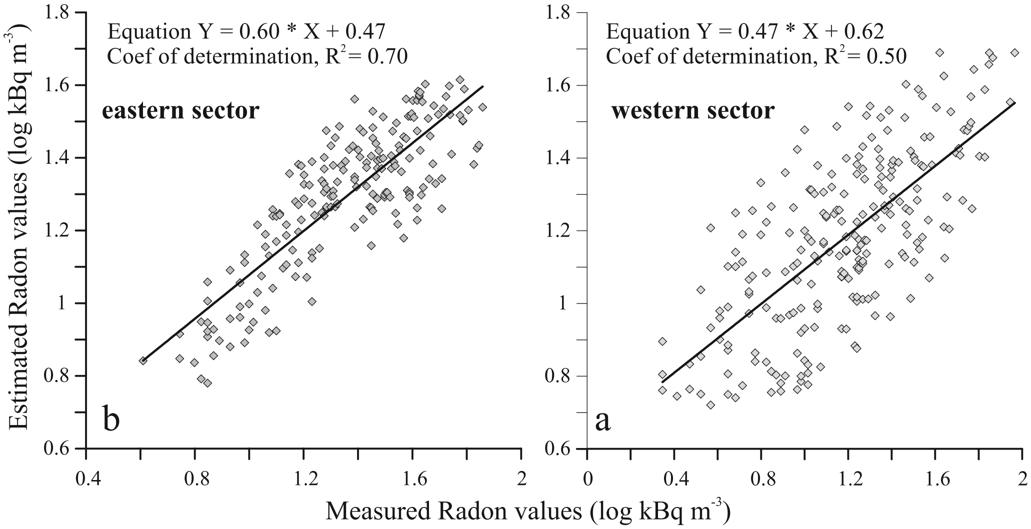

Figure 15. Scattergram of measured versus estimated values calculated in the cross-validation analysis. The interpolation line (continuous line) is very close to the theoretical line providing that the calculated model well fit with the data spatial behavior.

the selected variogram models for radon for the eastern (Figure 15a) and western (Figure 15b) sectors. The correlation coefficients of 0.7 for the data of the eastern sector and 0.5 for the data of the western sector indicate a good quality of the selected variogram model in the first case, as well as an acceptable selected variograms model in the second case, it means that only where sample density I low the error of the estimation could be higher (e.g., at the boundaries of the study area). Otherwise, considering that the environmental variables are often skewed is very difficult to obtain very high correlation coefficient of cross validation graphs.

[68] There is also a possibility of a smoothing effect of the kriging estimation, in this case a distinction needs to be made between a true nugget and a measurement error. If there is only small-scale variability (e.g., nugget effect) and no measurement error, then the repeated measurements at the same location would be identical. In this case the kriging variance is zero, e.g., exact interpolation. If the nugget represents a measurement error rather than a small-scale variability, repeated measurements at the same locations would be not perfectly correlated. This results in a predictor that does not exactly interpolate the data, but smoothes the measured data to account for the measurements errors.

[69] Radon and carbon dioxide anomalies (Figure 14) fit well with the trend of known structural features both in the eastern and western sectors, mimicking the general NW-SE (N305–310) fault orientation of the area. Higher Rn and CO_2 concentrations characterize the eastern sector of the Fucino Plain where the most active/recently activated faults (OF and SBGMF) occur. The shape of the anomalies confirms the highly anisotropic behavior shown by the experimental variograms and shows the spatial domain of the faults affecting the radon distribution.

[70] In the western sector radon distributions define the southern and the northern segments of the known Trasacco Fault (TF), in agreement with structural observations. This feature was observed in the field (F. Galadini, personal communication, 2004) to change along strike from brittle deformation in the SE, to ductile and less evident deformation (manifest as gentle surface undulations), to an area of no visible deformation to, finally, another zone of brittle deformation in the NW. This trend is clearly represented in the Rn contour map, going from a large, concentrated anomaly in the SE which decreases, disappears, and then returns as one moves to the NW. The elongation of anomalies agrees with local TF orientation and coincides with the main 135° (N305) anisotropy axis of the variogram map. Yet it is quite clear that the anomalies are smeared laterally, confirming the rotation of the anisotropy axis toward the E-W direction. In this sector this phenomenon is probably linked to a more complex fault geometry (wide fracturing) associated with a shallow structural high of carbonate substratum. Furthermore, in the northwestern sector of the plain very high radon anomalies clearly define the WSW-ENE ACF, as well as some associated minor Apenninic faults oriented toward the center of the plain.

[71] The CO_2 contour map shows low values with respect to the eastern sector, but an anomalies distribution similar to that of radon. The anomalies are located in correspondence with the TF and with the minor Apenninic faults in the northwester sector of the plain. Minor CO_2 anomalies are located in the center of the plain where fault-induced liquefaction was recognized during the Avezzano earthquake, and along a WSW-ENE buried fault.

[72] A W-E soil gas profile constructed along one of the seismic lines performed during a geophysical survey [*Cavinato et al.*, 2002] highlights a good correlation of Rn and CO_2 peaks with the fault traces obtained by the seismic data interpretation (Figure 16).

7. Discussion

[73] In general soil gas surveys exhibit different gas-bearing properties for faults bordering versus those cutting the Fucino Plain. This difference likely originates from features such as geometry (high angle, listric faults), seismic activity (seismogenic faults or faults related to surface

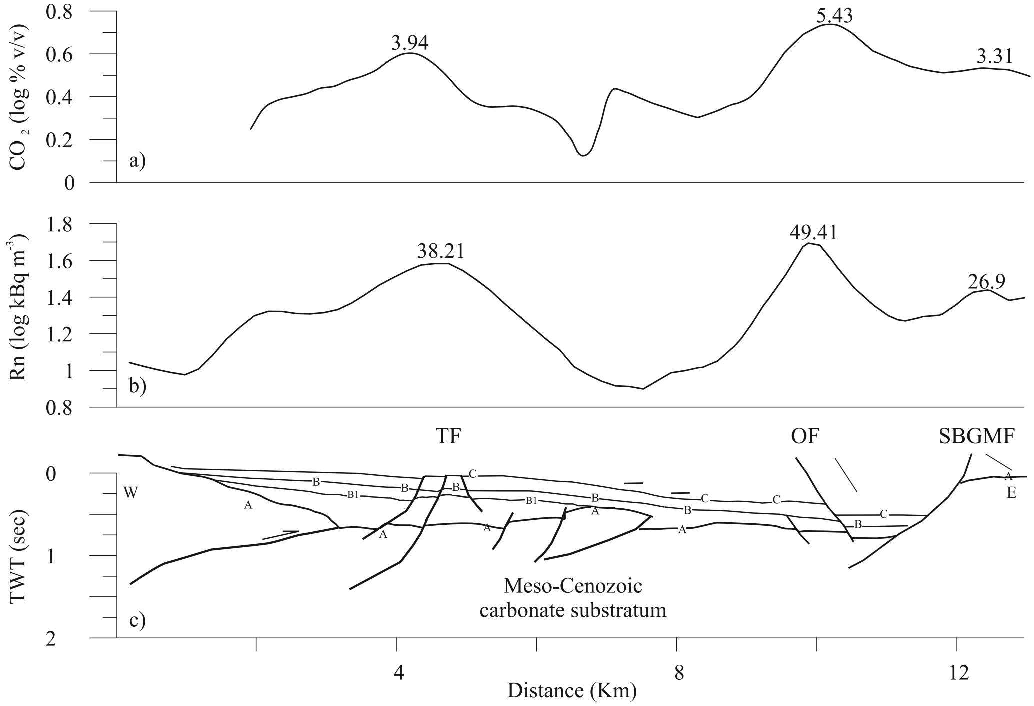

Figure 16. Soil gas and geological cross section profiles highlights a good correlation of Rn and CO_2 peaks with the fault traces obtained by the seismic data interpretation.

ruptures along changes of lithology), and depth (capable or blind faults). Soil gas anomalies are mainly clustered around specific locations or mark belts of enhanced permeability along the NW-SE direction, located along structural elements which are known or inferred on the basis of morphological interpretation or subsurface data, both in the eastern and in the western sectors of the Fucino Plain.

[74] Radon and carbon dioxide appear to better outline the structural features known and/or buried in the plain with respect to other studied gases. In particular, as shown in Figures 14a and 14b, gas anomalies clearly strike along the direction of the SBGMF, OF, and the N-S fault recognized by *Oddone* [1915] near the village of Pescina in the eastern sector while in the western sector anomalies also highlight the ACF and the southern part of the TF but show a more pervasive distribution.

[75] The strong Apennine anisotropy of the anomalies is linked to the spatial domain of the faults which are characterized by different geometries and depth. The SBGMF consists of NW-SE trending, 80°–90° dipping, dip-slip fault scarps that occur in fluvial and lacustrine gravels or silt. According to seismic interpretation and paleosismological data (G. P. Cavinato, personal communication, 2004), the fault is more than 5 km deep and about 12 km long, although it because less well defined when the scarps affect silty sediments. In contrast the OF is a buried structure only inferred by geometric-structural considerations and probably linked to the Alto-Sangro fault, which cuts the carbonate ridge to the south of Ortucchio. In this sector the thickness of the sedimentary cover is about 700–800 m.

[76] In the western sector the NW-SE trending TF runs for about 7 km across the inner portion of the basin. Paleoseismological trench studies and seismic profiles highlight a fault plane dipping 60° toward the SW up to a depth of about 1 km. In this sector of the plain the thickness of the sedimentary cover is of about 100–200 m [*Cavinato et al.*, 2002; *Cavinato and De Celles*, 1999; *Galadini and Galli*, 1999].

[77] Fault-related radon anomalies are unlikely to originate from a great depth because of the short half-life and low rate of subsurface diffusive migration of this gas [*Tanner*, 1980]. A probable crustal process for radon transport is linked to the existence of a naturally occurring microflux of gas ("geogas") which is enhanced along the recognized crustal faults. This microflow regards advective movement of a mixture of naturally occurring gases, formed by carrier gases (CO_2, CH_4, N_2) which transport rare gases (He, Rn) [*Morner and Etiope*, 2002; *Etiope and Lombardi*, 1995; *Malmqvist and Kristiansson*, 1984]. High Rn emissions are generally related to U-rich soils and bedrock; however, it is not rare to find soil gas Rn values above fault zones which are much higher than the level attributable to in situ U decay. The observed linear Rn trends of the anomalies cannot be accounted for by the very thin, discontinuous U and Ra-rich volcanic deposits scattered throughout the plain. As described above the ^{226}Ra content measured in soil samples collected throughout the plain is in equilibrium with a ^{222}Rn concentration of about 25 Bq L^{-1}. (see Figure 9a). Radon concentrations above this value generally occur along faults and provide evidence for trace gas transport from deeper source by a carrier gas, mainly CO_2, as shown in the carbon dioxide distribution map (Figure 14) and by the measured flux data (Figure 12). According to *Etiope and Martinelli* [2002] gas migration at relatively high speed can be due to (1) pressure-driven continuous gas-phase flow through dry fractures; (2) pressure-driven continuous gas phase displacing water in saturated fractures; and (3) buoyancy of gas bubbles in aquifers and water-filled fractures.

[78] The bubble movement has been theoretically and experimentally recognized as a fast gas migration mechanism [*Varhegyi et al.*, 1992]. The key parameters constraining validity of these types of advective gas migration is the intrinsic permeability of rocks and the fracture width.

[79] Excluding faulted and fractured rocks, crustal permeability is on the order of 10^{-20} to 10^{-16} m^2 [*Manning and Ingebritsen*, 1999]. In fault zones, at a regional scale, the permeability is higher than these values, and is much higher at local (m) scale in fractured rocks. In this case gas-phase migration involves water displacement and bubble flow. Considering that values of fracture aperture at depth vary from 10 to 100 μm for low-permeability saturated clays and in accordance with Stokes' law, theoretical gas velocity of bubble flow is in the range of 0.01–0.1 cm s^{-1} [*Etiope and Martinelli*, 2002].

[80] In this regard, the occurrence of bubbling (mainly CO_2 and CH_4) in some wells and drainage channels throughout the Fucino Plain suggest that large amounts of gas occur in basin aquifers. This suggests that in faulted zones near-surface gas oversaturation occurs and bubbles migrate to the surface of the water table. As such the trace gases may advect upward within bubbles consisting of more concentrated carrier gases such as CO_2 or CH_4, as supported by the similar soil gas distribution of Rn and CO_2 (Figure 14), and CH_4, Rn, and CO_2 exhalation values (Figure 12).

[81] Although the isotopic signatures ($\delta^{13}C_{CH4}$, $\delta^{13}C_{CO2}$, and $^3He/^4He$) to label the genetic processes of sampled gases are not available, the mainly biogenic origin of methane and carbon dioxide produced by degradation of organic matter in lacustrine sediments is a feasible mechanism (see Figure 10), even if the figure does not exclude partial dilution by deep origin CO_2. In fact, the presence in the plain of macroseepage phenomena, occurring as circular or elliptical areas of various sizes (gas vents) and enriched in CO_2 and CH_4, is usually indicative of underlying thermogenic gas reservoirs, leaking upward along discrete pathways (i.e., faults) through the softer and more deformable shallow cover sediments. Gas vents occur along the TF in the vicinity of the drainage channel, along the SBGMF near the villages of San Benedetto dei Marsi and Venere dei Marsi, and in the center of the plain (north of Borgo Ottomila) where liquefaction-induced deformations occur due to the presence of coseismic ruptures. The widely accepted explanation of this macroseepage is that gas pressure builds up in a shallow reservoir until a critical overpressurizing point is exceeded. Gas migration is thought to follow paths of least resistance and gas release is a sudden event, especially just before an earthquake (i.e., prewarning signal). In general, the linear arrangement of these spotty phenomena may define the strike of the underlying faults and fractures.

[82] Furthermore, the observation that Rn anomalies more effectively outline faults (re)activated during the 1915 earthquake (SBGMF and ACF) is consistent with an enhanced emanation power due to the fracturing and crushing phenomena induced by stress-strain related to the high seismicity of the plain. A possible mechanism is related to an increase of grain surface and porosity, as well as grain comminution by coseismic cracks, thereby producing high active surface area and circulation pathways, as well as high radon emanation rates [*Holub and Brady*, 1981].

[83] Helium distribution appears as spot anomalies that, in the western sector, match with the orientation of the TF (Figure 9c). Consistently, in this sector the spatial distribution of the high He values and their association with CO_2 and CH_4 anomalies could be indicative of gas microseepage from radiogenic/deep sources along this fault system. In this sector of the plain the presence of a buried structural high of the carbonate substratum suggests that the TF is a more complex structure that can act as a main route of migration for a deep geogas mix, though a likely prevailing radiogenic ^4He versus primordial ^3He could be hypothized.

[84] The medium to high permeability of sediments filling the basin in the westernmost sector probably affect the shallow soil gas distribution. In contrast the finer-grained, low-permeability and freshly faulted deposits on the eastern side of the plain result in transport channeling [*Ciotoli et al.*, 2005; *Lombardi et al.*, 1996], whereby high gas fluxes are confined along segments of discontinuities. Furthermore, the thickness of the sedimentary cover, which varies from about 150 m in the southwestern corner of the plain up to 800 m in the northeastern part, does not seem to affect soil gas migration and shallow distribution in faulted zones.

[85] The geostatistical analysis of radon and carbon dioxide concentrations greatly improved data interpretation, outlining different domains of spatial autocorrelation linked to the gas-bearing properties of faults bordering versus those cutting the Fucino Plain. The geostatistical approach provides a clear correlation between the shape and orientation of the gas anomalies, and the different geometry and geo-structural characteristics of the faults recognized in the western and eastern sectors of the plain.

[86] Fault geometry (simple high-angle dip-slip faults) and high seismic activity of the SBGMF and OF in the eastern sector of the plain produce the Apenninic elongation of shallow gas anomalies characterized by a high anisotropy ratio. In this sector the variogram analysis shows a main direction of anisotropy (N305–315) along the SBGMF and OF, and in this direction the spatial domain of the faults affect the soil gas distribution within a range of about 6 km. In contrast along the orthogonal direction the spatial domain of autocorrelation is very narrow and affects the shallow distribution of the gas anomalies according to a single-scale phenomenon (simple model variogram) within a range of about 1 km both for CO_2 and Rn. The high-resolution sampling (rectangular transect of 0.8 $\times$ 0.2 km), carried out along the minor axis of anisotropy (orthogonal to the SBGMF) near the village of San Benedetto dei Marsi, shows very high values of all gas species. The reason of these results, as described above, could be due to the fact that the sampling was conducted within the spatial domain of the fault and for a distance smaller than the calculated range (see Figure 13). This sampling did not, unfortunately, include the background values occurring beyond the influence of the structure, as indicated by the range of the variogram calculated along the minimum axis of anisotropy (Figure 13).

[87] In the western sector the broader distribution of the anomaly implies that the TF is not a simple planar (i.e., dip slip) structure like the SBGMF, but rather is wider fault system (i.e., listric fault) with complex geometry which has a wide fracture zone surrounding the main fault. In this

Table 3. Comparison Between Geological and Structural Information of the SBGMF and TF and the Summary Statistics of Soil Gas Samples Collected in a Buffer Area Around the Faults Identified by the Variogram Models

				Rn		CO_2		CH_4		He	
	Depth	Length	Cover Thickness	Median	Max	Median	Max	Median	Max	Median	Max
SBGMF	>5 km	12 km	800 m	24.4	119.5	3	15.2	1.6	27.6	5.2	6.1
TF	1.5 km	7 km	150 m	18.3	53.3	2.7	18.5	1.1	4.4	5.3	5.9

sector the variogram analysis shows two main directions of anisotropy: N305−315 along the main elongation of the TF and N85−90 along the orthogonal direction. In particular, the latter indicates that the TF fault system affects the shallow distribution of the gas anomalies in this direction according to a double-scale phenomenon (nested variogram): (1) at local scale with a range of 1.3 km for CO_2 and 2.25 km for Rn and (2) at regional scale with a range of 7 km for both gases.

[88] In particular, this fault has been observed in the field (F. Galadini, personal communication, 2004) to change from SE to NW along strike from brittle deformation, to ductile and less evident deformation (manifest as gentle surface undulations), to no visible deformation and to, finally, another zone of brittle deformation. This trend is represented quite clearly in the Rn and CO_2 soil gas contour maps, going from a large, concentrated anomaly in the SE which decreases, disappears, then returns as one moves to the NW. The elongation of anomalies agrees with local fault orientation and coincides with the main anisotropy axis. Yet it is quite clear that the anomalies are smeared laterally in the direction of the second anisotropy axis (E-W) due to the presence of a more complex fault geometry (i.e., diffuse fracturing). The different ranges for the two gases at local scale could be linked to their different geochemical behavior in the shallow environment: The carbon dioxide is more soluble in groundwater and more reactive than radon in the vadose zone, making it difficult to distinguish CO_2 anomalies from the background. In contrast, shallow fracturing could increase the production of radon, as well as aiding in its transport over a greater distances.

[89] High He concentrations occur in this sector relative to the eastern one. This could be linked both to U mobilization by active fluid circulation in the carbonate structural high, and to the presence of a thin sedimentary cover ranging from 100 to 200 m. Helium migration is enhanced by the action of the CO_2 and CH_4 carrier gases which characterize the bubbling phenomena in the drainage channel in the central part of the plain, and some gas vents located along the prolongation toward north of the TF. A comparison of soil gas concentrations (i.e., anomalies of CO_2, He, Rn, CH_4) relatively to some fault parameters (i.e., depth of structures, sizes, thickness of cover, etc.) is reported in Table 3.

[90] The results of the geostatistical analysis of soil gas data help create a schematic model showing how the spatial domain of faults with different geostructural features could affect shallow soil gas distributions. In fact, the variogram models of CO_2 and Rn data highlight a different spatial behavior within the western and eastern sector of the Fucino Plain (Figure 17). The proposed model can be tested by applying the same geostatistical technique to soil gas data in other areas of the Apennine chain with similar geological scenarios. Furthermore, the geostatistical analysis (i.e.,

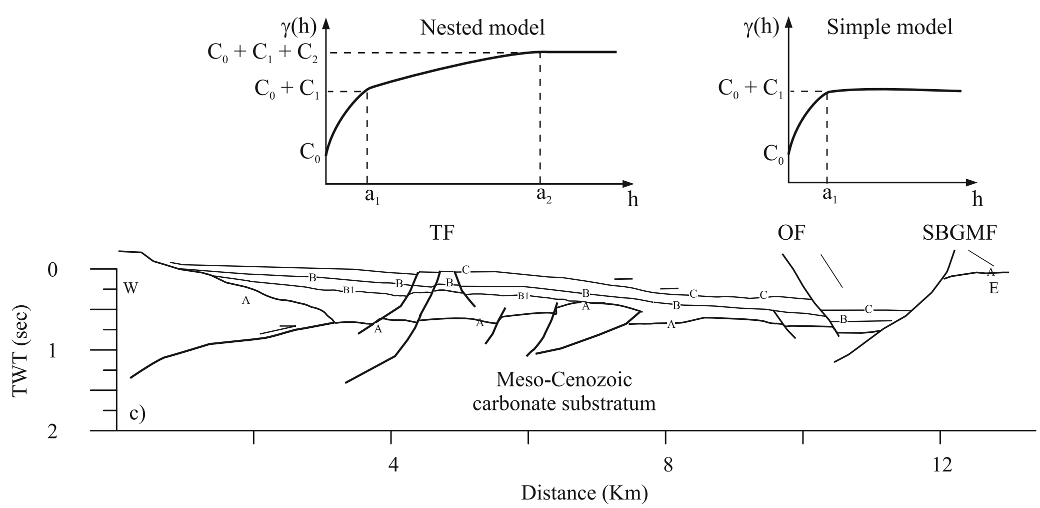

Figure 17. Sketch model of the shallow Rn spatial distribution inferred by the different variogram models calculated in the eastern and western sectors of the plain where faults with different geometries and activities were recognized. On the eastern sector the Rn and CO_2 spatial domains is well defined by a simple variogram model that agrees with the simple geometry of the SBGMF and OF (i.e., dip-slip faults). In contrast, the nested variogram model selected for the Rn and CO_2 data of the western sector may be the result of the complex geometry of the TF (i.e., listric fault), which has a wide fracture zone surrounding the main fault. The two types of variogram models are reported above the W-E oriented cross section (A-B in Figure 2) constructed by using data from seismic survey [*Cavinato et al.*, 2002].

Table 4. Main Statistical Parameters Calculated for Transects 1 and 3[a]

	Samples	Mean	Median	Min	Max	IQR	SD
			Luco dei Marsi Transect				
Rn, kBq m^{-3}	76	9.26	7.60	0.00	31.08	9.60	7.42
CO_2,%	76	2.80	2.40	0.02	9.04	2.80	2.04
CH_4, ppm	76	4.94	0.46	0.01	3.26	1.00	37.32
He, ppm	76	5.30	5.22	5.00	6.70	0.07	0.21
			San Benedetto Gioia dei Marsi Transect				
Rn, kBq m^{-3}	84	29.88	25.30	2.58	93.98	23.50	19.83
CO_2,%	84	3.47	3.00	0.10	17.15	3.00	2.83
CH_4, ppm	84	64.73	0.90	0.01	2520.00	1.50	131.40
He, ppm	84	5.28	5.30	4.70	6.20	0.27	0.25

[a]Transect 1 (Luco dei Marsi, 10–20 sample km^{-2}) and transect 3 (San Benedetto Gioia dei Marsi, 80–100 sample km^{-2}). Data show that the spreading of the variables, in general, increases with the sample density.

variography) quantified the spatial domain of anomalies in correspondence with different faults in terms of distances along the major/minor axes of anisotropy. This information will be useful for the planning of future samplings (i.e., directional high-resolution profiles, transects, etc.).

[91] In general, additional high-resolution samplings are often aimed at better delineating anomalous zones, but the decrease of the sampling grid size has the effect of increasing the spread of the variable (i.e., the interquartile range and the standard deviation increase). In contrast, as the sampling grid size increases the distribution gradually becomes more symmetric and thus the difference between the median and the mean becomes smaller. Statistical parameters calculated for Rn and CO_2 concentrations measured in samples collected in transects 1 and 3 show that the median, IQR and standard deviation increase as the sampling density increases (Table 4). This effect in the changes of the sampling grid size will be greatest for data sets in which data are spatially uncorrelated (i.e., variogram with high nugget).

[92] A by-product of kriging is the kriging variance. The kriging variance is a measure of estimate confidence and is a function of the variogram parameters and the sampling configuration. Observations are frequently obtained along a transect to provide data for this purpose. Once a representative variogram has been obtained and a model has been fitted the coefficients of the model can be used to compute the maximum kriging variance for different sample spacings. Contour plots of the kriging standard deviation can be used to delineate areas of large uncertainty in the kriging estimates. Further sampling from these locations can substantially improve the accuracy of predictions. In this work the kriging standard deviation maps show uncertainty in the kriging estimates only at the boundaries of the study area due to the low sampling density. Furthermore, it is worth to note that the reduced kriging errors are approximately normally distributed.

[93] It is then possible to ascertain the largest sample grid spacing that could be used to achieve the lowest kriging variance. If the variogram has a short range a fine grid needs to take advantage of spatial dependence (i.e., high cost/benefit ratio); if the variogram has long range a coarse grid will give similar results. In this study prediction locations are assumed not to coincide with measurements locations in this case no distinction needs between the nugget and the measurements error. Given a mean sample spacing (g) of 0.65 km and total area (A) of 220 km^2, the number of sample points (n) required to cover the area is calculated with

$$n = \left(\frac{\sqrt{A}}{g} + 1\right)^2 = \left(\frac{\sqrt{200}}{0.65} + 1\right)^2 = 576 \quad (3)$$

This number of samples corresponds remarkably well with the total number of samples actually collected in the preliminary regional survey.

[94] In exploration the final decision on additional sampling is based on the following criteria: (1) subareas with high values are more interesting than others; (2) high extension variance requires to reduce large sampling grids; and (3) high local variability require a denser sampling.

[95] The importance of these criteria may differ for different study sites. The calculation and plotting of the moving window statistics for variable values are a basis for the evaluation of the existing sampling pattern and support decision for locating additional samples (Figure 11) (some commercial GIS packages contain Voronoi tessellation modules, e.g., ARC/GIS 8.0, Esri Inc.). This can enhance the soil gas interpretation, especially when soil gas surveys are used for seismic microzonation or for gas hazard evaluation studies.

8. Conclusions

[96] The fundamental goal of this study is to detect evidence of deep origin fluids in the shallow environment which are due to gas ascent along enhanced permeability pathways, such as deep regional faults.

[97] Numerous soil gas measurements of four gaseous species with very different geochemical behaviors were performed in the Fucino Basin at different scales across known and inferred structural discontinuities. In the eastern sector of the Fucino Plain the relatively simple dip-slip geometry of the SBGMF and the OF (recently activated during the 1915 Avezzano earthquake, M_b = 7.0), affects the distribution of high Rn and CO_2 values according to a clear linear Apenninic trend. In contrast, on the western side of the plain the TF, an inferred listric fault which is not visible on surface, has lower radon and carbon dioxide values that are more diffusely distributed, but coupled with high values of helium.

[98] On the basis of these observations radon and carbon dioxide appear to be good tracers of faults (re)activated during the 1915 earthquake. The fact that the highest values are observed over the coseismic fractures may be an indication of the more open nature of these features and thus higher permeability. However, independent of gas origin, the results show that gases migrate preferentially through zones of brittle deformation by advective processes as a geogas mixtures, as suggested by the relatively high rate of migration needed to obtain anomalies of short-lived ^{222}Rn in the soil pores.

[99] A comprehensive statistical and geostatistical treatment of this data followed in order to provide insights into the spatial influence of tectonic discontinuities which affect deep-seated gas migration toward the surface. Geostatistical analysis greatly enhanced soil gas data interpretation and highlighted different gas-bearing properties for the various

faults. The results yielded anomalies with different shapes, reflecting the different gas-bearing properties and geometry of the eastern seismogenic faults (SBGMF, OF) and the buried structural system (TF) occurring in the western side of the Fucino Plain. In particular, the broader distribution of the anomalies around the TF implies that this is not a simple planar feature like the SBGMF, but rather is wider and highly fractured zone linked to the presence of a structural high of the carbonate substratum.

[100] The high-resolution sampling performed over detailed areas indicated that at the high-resolution scale the different contribution of phenomena acting along specific directions (i.e., fault-related anisotropy effect) versus phenomena acting randomly (i.e., isotropic background field) could be less apparent than at a regional scale. This may be due to the scale effect, when sampling is performed within the influence range of a structure (e.g., a fault), as occurs in the transect carried out across the SBGMF. In this case the geostatistical approach can be useful to greatly enhance the sampling strategy.

[101] In fact, the proposed methodology (soil gas prospecting coupled with the geostatistical analysis), provides (1) the quantification of the spatial domain of structural discontinuities, with different activity and/or geometry, on the shallow distribution of soil gases; (2) the relationships between the size of the target (i.e., regional faults) and the sampling design; and (3) the evaluation of the sampling pattern in the framework of future sampling schemes (i.e., the location of additional samples).

[102] This approach may constitute a good method of investigation and data interpretation, especially at local scale, in geohazard studies. This is particularly important here as the outlined scenario and some field observations indicate that the Fucino Plain may be prone to sinkhole formation.

[103] **Acknowledgments.** We are very grateful to S. E. Beaubien for revising the English of the manuscript. We are indebted to our technician Anna Baccani for her help in the laboratory. The research was partially funded by the European Community under the Environment and Climate Programme "Seismic Hazard Zonation: A Multidisciplinary Approach Using Fluid-Geochemistry Method" (GSZ) (ENV4-CT96-0291).

References

Åkerblom, G. (1993), Ground radon: Monitoring procedure in Sweden, paper presented at the "JAG" Disc. Meeting on Radon Workshop, Geology, Environment, Technology, R. Astron. Soc., London, 12 Feb.

Allard, P. (1986), Geochimie isotopique et origine de l'eau, du carbone et du soufre dans les gaz volcaniques: Zones de rift, marges continentales et arcs insulaires, thesis, Univ. Paris VIII Vincennes-Saint-Denis, Paris.

Andrews, J. N. (1983), Dissolved radioelements and inert gases in geothermal investigations, *Geothermics*, *12*(2)–(3), 67–82.

Annunziatellis, A., G. Ciotoli, S. Lombardi, and F. Nolasco (2003), Short and long term gas hazard: The release of toxic gases in the Alban Hills volcanic area (central Italy), *J. Geochem. Explor.*, *77*, 93–108.

Astorri, F., S. E. Beaubien, G. Ciotoli, and S. Lombardi (2002), An Assessment of gas emanation using GIS and geostatistics, *Health Phys.*, *82*(3), 358–366.

Azzaro, R., L. Ferreli, A. M. Michetti, L. Serva, and E. Vittori (1998), Environmental hazard of capable faults: The case of the Pernicana fault (Mt. Etna, Sicily), *Nat. Hazards*, *17*, 147–162.

Bally, A. W., L. Burbi, C. Cooper, and R. Ghelardoni (1986), Balanced sections and seismic reflection profiles across the central Apennines, *Mem. Soc. Geol. Ital.*, *35*, 257–310.

Baubron, J. C., P. Allard, J. C. Sabroux, D. Tedesco, and J. P. Toutain (1991), Soil gas emanations as precursory indicators of volcanic eruptions, *J. Geol. Soc. London*, *148*, 571–576.

Baubron, J. C., A. Rigo, and J. P. Toutain (2002), Soil gas profiles as a tool to characterise active tectonic areas: The Jaut Pass example (Pyrenees, France), *Earth Planet. Sci. Lett.*, *196*, 69–81.

Beaubien, S. E., G. Ciotoli, and S. Lombardi (2003), Carbon dioxide and radon gas hazard at the Alban Hill Area (central Italy), *J. Volcanol. Geotherm. Res.*, *123*, 63–80.

Birchard, G. F., and W. F. Libby (1978), Earthquake associated radon anomalies. Possible mechanisms, *Eos Trans. AGU*, *59*(4), 329.

Blumetti, A. M., A. M. Michetti, and L. Serva (1988), The ground effects of the Fucino earthquake of Jan. 13th, 1915: An attempt for the understanding of recent geological evolution of some tectonic structures, in *Historical Seismicity of Central-Eastern Mediterranean Region, Proceedings of the 1987 ENEA-IAEA International Workshop*, edited by C. Margottini and L. Serva, pp. 297–319, Nuove Teconol., l'Energie, e l'Ambiente, Rome.

Blumetti, A. M., F. Dramis, and A. M. Michetti (1993), Fault-generated mountain fronts in the Central Apennines (central Italy): Geomorphological features and seismotectonic implications, *Earth Surf. Processes Landforms*, *18*, 203–223.

Bosi, C., F. Galadini, and P. Messina (1995), Stratigrafia plio-pleistocenica della Conca del Fucino, *Quaternario*, *8*(1), 83–94.

Burghignoli, A., et al. (1991), Geotechnical characterization of Fucino clay, in *Proceedings of the 10th European Conference on Soil Mechanics and Foundation Engineering*, *Florence, Italy*, pp. 27–40, A. A., Balkema, Brookfield, Vt.

Cavinato, G. P., and P. G. De Celles (1999), Extensional basins in the tectonically bimodal central Apennines fault-thrust belt, Italy: Response to corner flow above a subducting slab in retrograde motion, *Geology*, *27*(10), 955–958.

Cavinato, G. P., C. Carusi, M. Dall'Asta, E. Miccadei, and T. Piacentini (2002), Sedimentary and tectonic evolution of Plio-Pleistocene alluvial lacustrine deposits of Fucino basin (central Italy), *Sediment. Geol.*, *148*, 29–59.

Chiles, J. P., and P. Delfiner (1999), *Geostatistics: Modeling Spatial Uncertainty*, 720 pp., John Wiley, Hoboken, N. J.

Ciotoli, G., and M. G. Finoia (2005), *Dalla Statistica Alla Geostatistica: Introduzione all'Analisi dei Dati Ambientali e Territoriali*, 440 pp., Aracne, Rome.

Ciotoli, G., M. Guerra, S. Lombardi, and E. Vittori (1998), Soil gas survey for tracing seismogenic faults: A case study in the Fucino Basin, central Italy, *J. Geophys. Res.*, *103*, 23,781–23,794.

Ciotoli, G., G. Etiope, M. Guerra, and S. Lombardi (1999), The detection of concealed faults in the Ofanto basin using the correlation between soil-gas fracture surveys, *Tectonophysics*, *299*(3)–(4), 321–332.

Ciotoli, G., S. Lombardi, S. Morandi, and F. Zarlenga (2005), A multidisciplinary statistical approach to study the relationships between helium leakage and neo-tectonic activity in a gas province: The Vasto Basin, Abruzzo-Molise (central Italy), *AAPG Bull.*, *88*(3), 355–372.

Deutsch, C. V., and A. G. Journel (1997), *GSLIB: Geostatistical Software Library and User's Guide*, 369 pp., Oxford Univ. Press, New York.

Duddridge, G. A., P. Grainger, and E. M. Durrance (1991), Fault detection using soil gas geochemistry, *Q.J. Eng. Geol.*, *24*, 427–435.

Durrance, E. M., and R. G. Gregory (1988), Fracture mapping in clays: Soil gas surveys at Down Ampney, Gloucestershire, *DOE Rep. DOE/RW/88081*, Dep. of Energy, Washington, D. C.

Eremeev, A. N., V. A Sokolov, and A. P. Solovov (1973), Application of helium surveying to structural mapping and ore deposit forecasting, in *Geochemical Exploration 1972*, edited by M. J. Jones, pp.183–192, Inst. of Min. and Metall., London.

Etiope, G., and S. Lombardi (1995), Evidence for radon transport by carrier gas through faulted clays in Italy, *J. Radioanal. Nucl. Chem.*, *193*(2), 291–300.

Etiope, G., and G. Martinelli (2002), Migration of carrier and trace gases in the geosphere: An overview, *Phys. Earth Planet. Inter.*, *129*, 185–204.

Etiope, G., M. Guerra, and A. Raschi (2005), Carbon dioxide and radon geohazards over a gas-bearing fault in the Siena graben (central Italy), *TAO*, *16*(4), 885–896.

Flexer, S., H. Wollenber, and A. Smith (1993), Distribution of radon sources and effects on radon emanation, in granitic soil at Ben Lomond, California, *Environ. Geol.*, *22*, 162–177.

Fridman, A. I. (1990), Application of naturally occurring gases as geochemical pathfinders in prospecting for endogenetic deposits, *J. Geochem. Explor.*, *38*, 1–11.

Galadini, F., and P. Galli (1999), The Holocene paleoearthquakes on the 1915 Avezzano earthquake faults (central Italy): Implication for active tectonics in the central Apennines, *Tectonophysics*, *308*, 143–170.

Galadini, F., and P. Messina (1994), Plio-Quaternary tectonics of the Fucino basin and surrounding areas (central Italy), *J. Geol.*, *56*(2), 73–99.

Galadini, F., P. Galli, and C. Giraudi (1997), Geological investigations of Italian earthquakes: New paleoseismological data from the Fucino Plain (central Italy), *J Geodyn.*, *24*(1)–(4), 87–103.

Giraudi, C. (1986), Faglie ad attività olocenica nella piana del Fucino, *Mem. Soc. Geol. Ital.*, *35*, 887–892.

Giraudi, C. (1989), Lake levels and climate for the last 30000 years in the Fucino area (Abruzzo, central Italy): A review, *Palaeogeogr. Palaeoclimatol. Palaeoecol.*, *70*, 249–260.

Goovaerts, P. (1997), *Geostatistics for Natural Resources Evaluation*, 477 pp., Oxford Univ. Press, New York.

Hauksson, E., and J. G. Goddard (1981), Radon earthquake precursor studies in Iceland, *J. Geophys. Res.*, *86*, 7037–7054.

Hickman, S., R. Sibson, and R. Bruhn (1995), Introduction to special section: Mechanical involvement of fluids in faulting, *J. Geophys. Res.*, *100*, 12,831–12,840.

Hinkle, M. (1994), Environmental conditions affecting concentrations of He, CO_2, O_2 and N_2 in soil gases, *Appl. Geochem.*, *9*, 53–63.

Holland, P. W., and D. E. Emerson (1990), The global helium-4 content of near-surface atmospheric air, in *Geochemistry of Gaseous Elements and Compounds*, pp. 97–113, Theophrastus, Athens.

Holub, R. F., and B. T. Brady (1981), The effect of stress on radon emanation from rock, *J. Geophys. Res.*, *86*, 1776–1784.

Houlding, S. W. (2000), *Practical Geostatistics: Modeling a Spatial Analysis*, 160 pp., Springer, New York.

Irwin, W. P., and I. Barnes (1980), Tectonic relation of carbon dioxide discharges and earthquakes, *J. Geophys. Res.*, *85*, 3115–3121.

Isaaks, E. H., and R. Mohan Srivastava (1989), *An Introduction to Applied Geostatistics*, 561 pp., Oxford Univ. Press, New York.

Journel, A. G. (1987), Geostatistics for the environmental sciences, *EPA Proj. Rep. CR 811893*, Environ. Protect. Agency, Environ. Monit. Syst. Lab., Las Vegas, Nev.

King, C. Y., B. S. King, W. C. Evans, and W. Zang (1996), Spatial radon anomalies on active faults in California, *Appl. Geochem.*, *11*, 497–510.

Klusman, R. W. (1993), *Soil Gas and Related Methods for Natural Resource Exploration*, 483 pp., John Wiley, New York.

Krajevskj, S. A., and B. L. Gibbs (1996), Understanding contouring. A practical guide to spatial estimation and contouring using a computer and basics of using variograms, 130 pp., Gibbs and Associates, Moorpark, Calif.

Krige, D. G. (1966), Two dimensional weighted moving average trend surfaces for ore-evaluation, *J. S. Afr. Inst. Min. Metall.*, *66*, 13–38.

Lombardi, S., and G. M. Reimer (1990), Radon and helium in soil gases in the Phlegrean Fields, central Italy, *Geophys. Res. Lett.*, *17*, 849–852.

Lombardi, S., et al. (1996), The refinement of soil gas analysis as a geological investigative technique, in *4th CEC R&D Programme on Management and Storage of Radioactive Waste (1990–1994)*, final report, *Nucl. Sci. Technol. Ser. EUR 16929*, 193 pp., Eur. Comm., Brussels.

Lombardi, S., et al. (1999), Seismic risk in the European Union, seismic hazard zonation: A multidisciplinary approach using fluid-geochemistry method (EC Contract ENV4–CT96–0291), in *Proceedings of the Review Meeting Held in Brussels on 27 and 28 November 1997*, edited by M. Yeroyanni, pp. 171–179, Eur. Comm. Dir.-Gen. Sci., Res. and Dev., Brussels.

Malmqvist, L., and K. Kristiansson (1984), Experimental evidence for an ascending microflow of geogas in the ground, *Earth Planet. Sci. Lett.*, *70*, 407–416.

Manning, C. E., and S. E. Ingebritsen (1999), Permeability of the continental crust: Implications of geothermal data and metamorphic systems, *Rev. Geophys.*, *37*, 127–150.

Matheron, G. (1971), The theory of regionalized variables and its applications, *Cah. 5*, Centre de Morphol. Math., Fontainebleau, France.

Matthews, M. D. (1985), Effects of hydrocarbon leakage on Earth surface materials, in *Unconventional Methods in Exploration for Petroleum and Natural Gas, IV*, edited by M. J. Davidson, pp. 27–44, South. Methodist Univ. Press, Dallas, Tex.

Michetti, A. M., F. Brunamonte, L. Serva, and E. Vittori (1996), Trench investigations of the 1915 Fucino earthquake fault scarps (Abruzzo, central Italy): Geological evidence of large historical events, *J. Geophys. Res.*, *101*, 5921–5936.

Morewood, N. C., and G. P. Roberts (2002), Surface observations of active normal fault propagation: Implications for growth, *J. Geol. Soc.*, *159*, 263–272.

Morner, N. A., and G. Etiope (2002), Carbon degassing from lithosphere, *Global Planet. Change*, *33*(1)–(2), 185–203.

Mostardini, F., and S. Merlini (1988), Appennino centro-meridionale: Sezioni geologiche e proposta di modello strutturale, *Mem. Soc. Geol. Ital.*, *35*, 177–202.

Nazaroff, W. M., and A. V. Nero (1988), Radon and its decay products in indoor air, John Wiley, Hoboken, N. J.

Oddone, G. (1915), Gli elementi fisici del grande terremoto marsicano-fucense del 13 gennaio 1915, *Boll. Soc. Sismol. Ital.*, *19*, 71–215.

Oliver, B. M., J. G. Bradley, and H. Farrar IV (1984), Helium concentration in the Earth's lower atmosphere, *Geochim. Cosmochim. Acta*, *48*, 1759–1767.

Oliver, M., R. Webster, and J. Gerrad (1989), Geostatistics in physical geography. part I: Theory, *Trans. Inst. Br. Geogr.*, *14*, 259–269.

Pannatier, Y. (1996), *Variowin: Software for Spatial Data Analysis in 2D*, 91 p., Springer, New York.

Pogorsky, L. A., and G. S. Quirt (1981), Helium emanometry in exploring for hydrocarbons, part I, in *Unconventional Methods in Exploration for Petroleum and Natural Gas II*, pp. 124–135, South. Methodist Univ. Press, Dallas, Tex.

Reimer, G. M. (1990), Reconnaissance techniques for determining soil-gas radon concentrations: An example from Prince Georges County, Maryland, *Geophys. Res. Lett.*, *17*, 809–812.

Roberts, G. P., A. M. Michetti, P. Cowie, N. C. Morewood, and I. Papanikolaou (2002), Fault slip-rate variations during crustal-scale strain localisation, central Italy, *Geophys. Res. Lett.*, *29*(8), 1168, doi:10.1029/2001GL013529.

Roberts, G. P., P. Cowie, I. D. Papanikolaou, and A. M. Michetti (2004), Fault scaling relationships, deformation rates and seismic hazards: An example from Lazio-Abruzzo, central Italy, *J. Struct. Geol.*, *26*, 377–398.

Schroeder, G. L., H. W. Kraner, and R. D. Evans (1965), Diffusion of radon in several naturally occurring soil types, *J. Geophys. Res.*, *70*, 471–474.

Segovia, N., J. L. Seidel, and M. Monnin (1987), Variations of radon in soils induced by external factors, *J. Radioanal. Nucl. Chem. Lett.*, *119*, 199–209.

Shapiro, M. H., J. D. Melvin, T. A. Tombrello, J. Fong-Liang, L. Gui-Ru, and M. H. Mendenhall (1982), Correlated radon and CO_2 variations near the San-Andreas fault, *Geophys. Res. Lett.*, *9*, 503–506.

Sibson, R. H. (1990), Faulting and fluid flow, in *Short Course on Fluids in Tectonically Active Regions of the Continental Crust*, edited by B. E. Nesbitt, *Mineral. Assoc. Can. Handb.*, *18*, 93–132.

Sinclair, A. J. (1991), A fundamental approach to threshold estimation in exploration geochemistry: Probability plots revisited, *J. Geochem. Explor.*, *41*, 1–22.

Slemmons, D. B., and R. McKinney (1977), Definition of "active fault", *Misc. Pap. S-77-8*, final report, 22 pp., U. S. Army Eng. Waterways Exp. Stn., Vicksburg, Miss.

Sokolov, V. A. (1971), *Geochemistry of Natural Gases*, Niedra, Moscow.

Stein, M. L. (1999), *Interpolation of Spatial Data: Some Theory From Kriging*, 250 pp., Springer, New York.

Stranden, E., A. K. Kolstad, and B. Lind (1984), The influence of moisture and temperature on radon exhalation, *Radiat. Protect. Dosimetry*, *7*, 55–58.

Strong, K. P., and D. M. Levins (1982), effect of moisture content on radon emanation from uranium ore and tailings, *Health Phys.*, *42*, 27–32.

Sugisaki, R. (1983), Origin of hydrogen and carbon dioxide in fault gases and its relation to fault activity, *J. Geol.*, *91*, 239–258.

Sugisaki, R., H. Anno, M. Aedachi, and H. Ui (1980), Geochemical features of gases and rocks along active faults, *Geochem. J.*, *36*, 101–112.

Tanner, A. B. (1980), Radon migration in the ground: A supplementary review, in *The Natural Radiation Environment, I*, edited by T. F. Gesell and W. M. Lowder, pp. 5–56, Univ. of Tex., Austin.

Tobler, W. (1970), A computer movie simulating urban growth in the Detroit region, *Econ. Geogr.*, *46*, 234–240.

Toutain, J. P., and J. C. Baubron (1999), Gas geochemistry and seismotectonics: A review, *Tectonophysics*, *304*, 1–27.

Varhegyi, A., J. Hakl, M. Monnin, J. P. Morin, and J. L. Seidel (1992), Experimental study of radon transport in water as test for transportation microbubble model, *J. Appl. Geophys.*, *29*, 37–46.

Vittori, E. (1994), Project of map and database of active fault in Italy: Methodological approach, in *Proceedings of Scientific Meeting on the Seismic Protection*, edited by V. Spagna, pp. 119–130, Giunta Reg. del Veneto, Palazzo Balbi, Venice, Italy.

Vittori, E., L. Serva, and S. Sylos Labini (1991), Palaeoseismology: Review of the state-of-the-art, *Tectonophysics*, *193*, 9–32.

Wang, C., X. Li, and B. Wei (1991), *Applications of Measurement of Fracture Gases in Seismological Sciences* (in Chinese), Seismol. Press, Beijing.

Ward, S. N., and G. Valensise (1989), Fault parameters and slip distribution of the 1915 Avezzano, Italy, earthquake derived from geodetic observations, *Bull. Seismol. Soc. Am.*, *79*, 690–710.

Washington, J. W., and A. W. Rose (1992), Temporal variability of radon concentration in the interstitial gas of soils in Pennsylvania, *J. Geophys Res.*, *97*, 9145–9159.

Zhang, X., and D. J. Sanderson (1996), Numerical modeling of the effects of fault slip on fluid flow around extensional faults, *J. Struct. Geol.*, *18*, 109–119.

Zhiguan, S. (1991), A study on the origin of fault gases in western Yunnan, *Earthquake Res. China*, *5*(1), 45–52.

A. Annunziatellis, G. Ciotoli, and S. Lombardi, Dipartimento di Scienze della Terra, Università di Roma "La Sapienza," Place Aldo Moro 5, I-00185 Rome, Italy. (giancarlo.ciotoli@uniroma1.it)